

# A basic model for high energy cosmic ray interactions

Sergey Ostapchenko<sup>1</sup>, Tanguy Pierog<sup>2</sup> and Günter Sigl<sup>1</sup>

<sup>1</sup>*Universität Hamburg, II Institut für Theoretische Physik, 22761 Hamburg, Germany*

<sup>2</sup>*Institute for Astroparticle Physics, Karlsruher Institut für Technologie,  
Hermann-von-Helmholtz-Platz 1, 76344 Eggenstein-Leopoldshafen, Germany*

March 16, 2026

## Abstract

A Monte Carlo generator of high energy cosmic ray interactions, relying on a very basic and transparent theoretical formalism, in the framework of the Reggeon Field Theory, is presented. The main motivation for our work is to provide a new cosmic ray interaction model characterized by relatively transparent physics, sufficient parameter freedom, and a high computational efficiency, which can be easily managed by external users, including a re-tuning of the model parameters. Such a model can be used for studying potential modifications of the interaction treatment, necessary for describing particular sets of data on extensive air showers initiated by high energy cosmic rays, at a microscopic level, thereby keeping a consistency with general restrictions, like the unitarity, energy-momentum and charge conservation, Lorentz and isospin invariance. Importantly, this should allow one to study a compatibility of such modifications with relevant accelerator data. The model results for particle production and for basic extensive air shower characteristics are presented and discussed.

## 1 Introduction

Studies of ultra high energy cosmic rays (UHECRs) are traditionally performed using indirect detection techniques: inferring the properties of primary cosmic ray (CR) particles from measured characteristics of so-called extensive air showers (EAS) – nuclear-electromagnetic cascades initiated by interactions of primary CRs in the atmosphere of the Earth [1, 2]. Consequently, such experimental activities imply an extensive use of numerical modeling of EAS development. A special role in EAS simulations is played by Monte Carlo (MC) generators of hadronic interactions, which form a bridge from accelerator experiments studying such interactions in great detail to the CR field and which are responsible for the description of EAS backbone – the cascade of nuclear interactions of both primary CRs and of produced secondary hadrons in the atmosphere [3]. MC generators of CR interactions have been considerably improved over the past decades, reaching a high level of sophistication [4, 5, 6], while the parameters of those models have been tuned based on a variety of accelerator data.

However, recent UHECR studies revealed that a number of experimental observations can not be consistently described using present CR interaction models [7, 8, 9, 10]. Because of their considerable complexity, such models are typically regarded by experimental groups as “black boxes”, since a retuning of model parameters by external users has not generally been envisaged. This motivated one to consider an *ad hoc* rescaling of the predictions of EAS simulations for particular air shower observables (e.g., [11, 12]): to approach the experimental observations. While

providing useful hints on how the simulations should be changed in order to better describe the EAS data, such a practice is potentially dangerous for a number of reasons. First of all, doing so one neglects correlations between different EAS observables, which follow from a microscopic description of the interaction process. Secondly and perhaps more importantly, proceeding that way one is unable to check whether the desirable modifications are sensible in view of existing ample experimental data on the properties of hadron-proton and hadron-nucleus (nucleus-nucleus) collisions at high energies. Moreover, certain extreme modifications may come into conflict with basic conservation laws.

All of the above motivated us to develop a new relatively simple MC generator of hadronic interactions, staying within a very basic interaction picture, while using a reasonable and transparent formalism, within the Reggeon Field Theory (RFT) approach [13, 14]. Physics-wise, we are essentially coming back to the concepts of the original Quark-Gluon String and Dual Parton models [15, 16]. Therefore we use the name QGSb [Quark-Gluon Strings (basic)] for our model. In more detail, we employ a phenomenological formalism, describing hadronic and nuclear scattering as mediated by Pomeron exchanges. We consider contributions to the scattering amplitude from two kinds of Pomerons – corresponding to the underlying soft and semihard parton cascades. To extend the range of applicability of the model towards low energies, we take into consideration secondary Reggeon exchanges, using the “effective Reggeon” approach [17]. Production of secondary hadrons is treated as arising from fragmentation of strings of color field, stretched between constituent partons of interacting hadrons (nuclei).

It is worth stressing that we neither employ any microscopic treatment for parton cascades nor consider explicitly any nonlinear corrections. Rather, we assume that the effects of both are effectively accounted for in our two-component Pomeron amplitude, in what concerns predictions for EAS characteristics. However, this restricts the range of applicability of the model. Without an explicit treatment of perturbative parton cascades, one is unable to describe correctly the production of hadrons at large transverse momenta. On the other hand, without an explicit treatment of nonlinear interaction effects, the model is inapplicable for treating heavy ion collisions. While both limitations are insignificant for EAS applications, they pose restrictions on accelerator data sets which can be used for the calibration of the model.

To some extent, the proposed model is complementary to existing more sophisticated MC generators of CR interactions. Restraining from using advanced theoretical approaches regarding the treatment of various aspects of hadronic collisions, we are unable to take into consideration certain important constraints, most notably, ones arising from experimental measurements of structure functions of hadrons. Such a strategy is intentional since we aim at a higher flexibility of the model, compared to more advanced MC generators which are typically overconstrained, within a particular theoretically advanced but yet phenomenological approach.

The main motivation for our work is twofold. Firstly, we wish to have a model characterized by a sufficient parameter freedom, constrained mainly by accelerator data, as a basic framework for studying uncertainties for EAS predictions. Secondly and more importantly, we want to provide experimental teams with a MC generator characterized by relatively transparent physics and a sufficient parameter freedom, which can be used for studying potential modifications of the interaction treatment, necessary for describing particular sets of EAS data, at a microscopic level, thereby keeping a consistency with general restrictions, like the unitarity, energy-momentum and charge conservation, Lorentz and isospin invariance. The goal is to allow the experimentalists to check the “cost” of describing particular EAS data sets, in terms of (in)consistency with accelerator data.

Here we present the first version of the QGSb MC generator, designed to treat hadronic interactions in a broad energy range: from  $\sim 10$  GeV laboratory (lab.) energy up to the highest energies of cosmic rays observed ( $\sim 10^{11}$  GeV lab.). In the course of its development, we used and suitably adapted various relevant technical procedures of the QGSJET(-II/III) models [18, 19, 20]. The outline of the paper is as follows. In Section 2, we discuss the basic physics underlying our approach. In Section 3, the expressions for hadronic interaction cross sections are provided, while

Section 4 is devoted to a description of the treatment of secondary particle production. The results of the model for various characteristics of hadron-proton and hadron-nucleus collisions are presented in Section 5, in comparison to accelerator data. In Section 6, the energy dependence of basic EAS characteristics, predicted by the model, is presented and discussed. Finally we conclude in Section 7.

## 2 Basic physics

High energy hadronic collisions are predominantly multiple scattering processes, being mediated by (generally nonperturbative) parton cascades developing between the interacting projectile and target hadrons (nuclei). For such parton cascades, we use an effective macroscopic description – treating them as Pomeron exchanges. Here we have to take into account two mechanisms which impact the “parton content” of the Pomeron. First, with increasing energy, the contribution of the so-called semihard processes corresponding to parton cascades developing, at least partly, in the domain of high parton virtualities  $q^2$  becomes important – since the smallness of the corresponding strong coupling,  $\alpha_s(q^2)$ , in such cascades becomes compensated by large collinear and infrared logarithms and by a high parton density [21]. Instead of treating such perturbative cascades explicitly, we consider two contributions to the Pomeron amplitude: the one corresponding to “soft” (low virtuality) parton cascade, characterized by a rather slow energy rise, and the “semihard” one quickly rising with energy [22, 23]. Further, at sufficiently high energies, an important role in the interaction dynamics is played by nonlinear effects arising from “splitting” and “fusion” of parton cascades, both real and virtual ones, typically described as Pomeron-Pomeron interactions (e.g., [24]). Here we assume that the main consequence of such nonlinear corrections is to “renormalize” the Pomeron amplitude [25], yielding, in particular, a small intercept of the “soft” Pomeron component, corresponding to the above-mentioned slow energy rise of the corresponding contribution. Thus, we expect that our two-component Pomeron amplitude effectively takes into account the effects of both mechanisms: the perturbative parton cascading and the nonlinear corrections to the interaction dynamics, in what concerns the predictions for EAS characteristics.

In order to extend the model for a description of hadronic interactions at relatively low energies, below 100 GeV lab., one has to account for secondary Reggeon exchanges, in addition to the Pomeron contributions (e.g., [26]). In that respect, we follow the approach proposed in [17]: considering an exchange of a single effective Reggeon per reaction type, rather than treating explicitly all the relevant Reggeon contributions.

When describing high energy hadronic collisions, it is important to take into consideration inelastic diffraction processes and the closely related inelastic screening (“color fluctuation”) effects [14, 27]. To treat low mass diffractive excitations of interacting hadrons (nucleons), we rely on the Good-Walker (GW) approach [28]: considering hadrons to be represented by superpositions of a large number of Fock states characterized by different transverse sizes and by different couplings to the Pomerons, which diagonalize the scattering matrix, assuming a coupling to be proportional to the transverse area of the state. It is noteworthy that this mechanism gives rise to three important effects: a milder energy rise of the interaction cross sections, compared to the case when such inelastic screening corrections are neglected, especially, for hadron-nucleus and nucleus-nucleus collisions, the emergence of low mass diffraction, and larger fluctuations for secondary particle production. Regarding a treatment of high mass diffraction, a self-consistent approach implies an all-order resummation of enhanced Pomeron diagrams [29]. Here we rely instead on an effective description: considering only the diffractive cut of the simplest triple-Pomeron graph corresponding to an interaction between three “soft” Pomerons, as described in Section 4.

Having defined the Pomeron exchange amplitude, including the Pomeron coupling to various Fock states, one can calculate total, elastic, and inelastic cross sections for hadron-proton, hadron-nucleus, and nucleus-nucleus collisions. Moreover, considering unitarity cuts of the corresponding elastic scattering diagrams and applying the so-called Abramovskii-Gribov-Kancheli cutting rules

[30], one is able to obtain partial cross sections for various inelastic final states corresponding to having precisely  $n$  “elementary” production processes ( $n$  “cut Pomerons”), hence, to sample “macro-configurations” of the collisions, using MC methods. However, for treating secondary particle production, one has to define the hadronization procedure. In that respect, we traditionally assume that each cut Pomeron corresponds to a creation of a pair of strings of color field, stretched between constituent partons [(anti)quarks or (anti)diquarks] of the interacting hadrons [15, 16]. With such partons flying apart, the strings break up and hadronize via a creation of quark-antiquark and diquark-antidiquark pairs from the vacuum. Here we employ the string fragmentation procedure of the QGSJET model [18], the current implementation being described in [20]. While the parameters of this procedure can be expressed via intercepts of relevant Regge trajectories [31], we shall generally treat them as adjustable ones. In particular, since one expects important differences between soft and semihard parton cascades, notably, a higher parton density per unit rapidity for the latter, the string fragmentation parameters will generally differ between the soft and semihard Pomerons.

Apart from secondary hadron production, of importance for extensive air shower simulations is a treatment of the fragmentation of the nuclear spectator part composed of all noninteracting nucleons, in nucleus-nucleus collisions: since this impacts fluctuations of nucleus-induced EAS [18, 32]. Such a nuclear breakup is modeled using the percolation-evaporation approach of the QGSJET model [18].

### 3 Cross section formulas

#### 3.1 High energy collisions

The Pomeron exchange eikonal (the imaginary part<sup>1</sup> of the corresponding amplitude in the impact parameter representation) for hadron-proton collisions is usually chosen in the form

$$\chi_{hp}^{\mathbb{P}}(s, b) = \frac{\gamma_h \gamma_p (s/s_0)^{\alpha_{\mathbb{P}}(0)-1}}{R_h^2 + R_p^2 + \alpha'_{\mathbb{P}} \ln(s/s_0)} \exp\left[-\frac{b^2/4}{R_h^2 + R_p^2 + \alpha'_{\mathbb{P}} \ln(s/s_0)}\right], \quad (1)$$

where  $\alpha_{\mathbb{P}}(0)$  and  $\alpha'_{\mathbb{P}}$  are, respectively, the intercept and the slope of the Pomeron Regge trajectory,  $\gamma_h$  is the residue and  $R_h^2$  is the slope for Pomeron coupling to hadron  $h$ , and  $s_0 \simeq 1 \text{ GeV}^2$  – the hadronic mass scale;  $s$  and  $b$  are, respectively, the center-of-mass (c.m.) energy squared and the impact parameter for the collision.

As discussed in Section 2, we shall consider contributions to  $\chi_{hp}^{\mathbb{P}}$  from soft and semihard Pomerons, characterized by different energy dependence, i.e., by different overcriticalities (intercept minus unity)  $\Delta_s$  and  $\Delta_{sh}$ , and by different couplings to hadrons. We also assume hadron states to be composed of a number of GW components:

$$|h\rangle = \sum_{i=1}^{N_{\text{GW}}} \sqrt{C_h^{(i)}} |i\rangle, \quad (2)$$

where  $C_h^{(i)}$  are the corresponding partial weights ( $\sum_i C_h^{(i)} = 1$ ) and  $N_{\text{GW}}$  is the total number of GW states considered per hadron.

Thus, a Pomeron exchange between Fock states  $|i\rangle$  and  $|j\rangle$  of the projectile hadron and of the target proton, respectively, will be described by the eikonal

$$\chi_{hp(ij)}^{\mathbb{P}}(s, b) = \frac{\gamma_{h(i)} \gamma_{p(j)} (\delta_{s/sh} s^{\Delta_s} + (1 - \delta_{s/sh}) s^{\Delta_{sh}})}{R_{h(i)}^2 + R_{p(j)}^2 + \alpha'_{\mathbb{P}} \ln s} \exp\left[-\frac{b^2/4}{R_{h(i)}^2 + R_{p(j)}^2 + \alpha'_{\mathbb{P}} \ln s}\right]. \quad (3)$$

---

<sup>1</sup>The real part of the Pomeron amplitude can be neglected in the high energy limit.

Here  $\gamma_{h(i)}$  and  $R_{h(i)}^2$  are the residue and the slope for Pomeron coupling to Fock state  $|i\rangle$  of hadron  $h$ , while  $\delta_{s/sh}$  characterizes the relative weights of the soft and semihard Pomerons, which is related to a weaker coupling of the latter to hadrons. This is assumed to be universal for all hadron types and for all Fock states. Further, we use here the same slope  $\alpha'_{\mathbb{P}}$  for the soft and semihard Pomerons, i.e., we assume the same rate of transverse expansion for the corresponding underlying parton cascades. Generally, this might not be the case since a semihard cascade develops partly in a high parton virtuality  $q^2$  domain, where parton transverse displacements  $\Delta b^2 \propto 1/q^2$  are small, which may result in a smaller Pomeron slope.

Using the eikonals (3), one obtains for the total and elastic hadron-proton cross sections:

$$\sigma_{hp}^{\text{tot}}(s) = 2 \int d^2b \sum_{i,j} C_h^{(i)} C_p^{(j)} \left[ 1 - e^{-\chi_{hp(ij)}^{\mathbb{P}}(s,b)} \right] \quad (4)$$

$$\sigma_{hp}^{\text{el}}(s) = \int d^2b \left[ \sum_{i,j} C_h^{(i)} C_p^{(j)} (1 - e^{-\chi_{hp(ij)}^{\mathbb{P}}(s,b)}) \right]^2. \quad (5)$$

In turn, for the ‘‘topological’’ cross section corresponding to having precisely  $n$  elementary production processes (cut Pomerons), one has

$$\sigma_{hp}^{(n)}(s) = \int d^2b \sum_{i,j} C_h^{(i)} C_p^{(j)} \frac{\left[ 2\chi_{hp(ij)}^{\mathbb{P}}(s,b) \right]^n}{n!} e^{-2\chi_{hp(ij)}^{\mathbb{P}}(s,b)}. \quad (6)$$

The total inelastic cross section,  $\sigma_{hp}^{\text{inel}} = \sigma_{hp}^{\text{tot}} - \sigma_{hp}^{\text{el}}$ , consists of the ‘‘absorptive’’ part,

$$\sigma_{hp}^{\text{abs}}(s) = \sum_{n=1}^{\infty} \sigma_{hp}^{(n)}(s) = \int d^2b \sum_{i,j} C_h^{(i)} C_p^{(j)} \left[ 1 - e^{-2\chi_{hp(ij)}^{\mathbb{P}}(s,b)} \right], \quad (7)$$

and of the cross section for low mass diffraction. The latter splits into the projectile, target, and double diffraction cross sections:

$$\sigma_{hp}^{\text{SD(proj)}}(s) = \int d^2b \sum_{i,k,j,l} (C_h^{(i)} \delta_{ik} - C_h^{(i)} C_h^{(k)}) C_p^{(j)} C_p^{(l)} e^{-\chi_{hp(ij)}^{\mathbb{P}}(s,b) - \chi_{hp(kl)}^{\mathbb{P}}(s,b)} \quad (8)$$

$$\sigma_{hp}^{\text{SD(targ)}}(s) = \int d^2b \sum_{i,k,j,l} C_h^{(i)} C_h^{(k)} (C_p^{(j)} \delta_{jl} - C_p^{(j)} C_p^{(l)}) e^{-\chi_{hp(ij)}^{\mathbb{P}}(s,b) - \chi_{hp(kl)}^{\mathbb{P}}(s,b)} \quad (9)$$

$$\sigma_{hp}^{\text{DD}}(s) = \int d^2b \sum_{i,k,j,l} (C_h^{(i)} \delta_{ik} - C_h^{(i)} C_h^{(k)}) (C_p^{(j)} \delta_{jl} - C_p^{(j)} C_p^{(l)}) e^{-\chi_{hp(ij)}^{\mathbb{P}}(s,b) - \chi_{hp(kl)}^{\mathbb{P}}(s,b)}. \quad (10)$$

A generalization of Eqs. (4-10) for hadron-nucleus and nucleus-nucleus collisions can be found in [18, 33]. In particular, for the total and particle production cross sections for hadron-nucleus interactions, one has

$$\sigma_{hA}^{\text{tot}}(s) = 2 \int d^2b \sum_i C_h^{(i)} \left\{ 1 - \left[ \int d^2\kappa T_A(\kappa) \left( 1 - \sum_j C_p^{(j)} \Gamma_{hp}^{(ij)}(s, |\vec{b} - \vec{\kappa}|) \right) \right]^A \right\} \quad (11)$$

$$\begin{aligned} \sigma_{hA}^{\text{prod}}(s) &= \int d^2b \sum_{i,k} C_h^{(i)} C_h^{(k)} \left\{ 1 - \left[ \int d^2\kappa T_A(\kappa) \left( 1 - \sum_j C_p^{(j)} \Gamma_{hp}^{(ij)}(s, |\vec{b} - \vec{\kappa}|) \right) \right. \right. \\ &\quad \left. \left. \times \left( 1 - \sum_l C_p^{(l)} \Gamma_{hp}^{(kl)}(s, |\vec{b} - \vec{\kappa}|) \right) \right]^A \right\}. \end{aligned} \quad (12)$$

Here  $\Gamma_{hp}^{(ij)}$  is the profile function for a scattering of Fock state  $|i\rangle$  of the projectile hadron on Fock state  $|j\rangle$  of a target nucleon,

$$\Gamma_{hp}^{(ij)}(s, b) = 1 - e^{-\chi_{hp}^{(ij)}(s, b)}, \quad (13)$$

while  $T_A$  is the nuclear profile expressed via the nuclear density  $\rho_A$  as

$$T_A(r_\perp) = \int dz \rho_A(\vec{r}). \quad (14)$$

As discussed in Section 2, we assume the Pomeron couplings to different Fock states of hadrons to be proportional to the transverse radii squared of those states:

$$\gamma_{h(i)} = g_0 R_{h(i)}^2, \quad (15)$$

with  $g_0$  being thus (up to a factor) the coupling per unit transverse area. Further, to reduce the number of adjustable parameters, we consider equal weights for the different Fock states,

$$C_h^{(i)} \equiv 1/N_{\text{GW}}, \quad (16)$$

and choose a loguniform distribution for  $R_{h(i)}^2$ :

$$R_{h(i)}^2 = R_{h(1)}^2 d_h^{\frac{i-1}{N_{\text{GW}}-1}}. \quad (17)$$

Thus, in the minimal scheme described above, a treatment of proton-proton and proton-nucleus (nucleus-nucleus) collisions involves 7 adjustable parameters:  $\Delta_s$ ,  $\Delta_{\text{sh}}$ ,  $\alpha'_{\mathbb{P}}$ ,  $\delta_{s/\text{sh}}$ ,  $g_0$ ,  $R_{p(1)}^2$ , and  $d_p$ , which can be fixed using experimental data on the total, elastic, and diffractive proton-proton cross sections. Considering also interactions of pions and kaons, one has additionally the parameters  $R_{\pi(1)}^2$ ,  $R_{K(1)}^2$ ,  $d_\pi$ , and  $d_K$ , whose values can be fixed based on measured pion-proton and kaon-proton cross sections. It is worth discussing the basic correspondence between these parameters and experimental observables. The values of the overcriticalities  $\Delta_s$  and  $\Delta_{\text{sh}}$  have the largest impact on the energy dependence of the total, elastic, and inelastic cross sections at “intermediate” and very high energies, respectively, while the parameter  $\delta_{s/\text{sh}}$  controls the energy where the transition between the two trends takes place.<sup>2</sup> The Pomeron slope  $\alpha'_{\mathbb{P}}$  governs the shrinkage of the diffractive cone, being largely constrained by measurements of the proton elastic scattering slope,  $B_{pp}^{\text{el}} = d \ln d\sigma_{pp}^{\text{el}}/dt|_{t=0}$ . The other parameters,  $g_0$ ,  $R_{p(1)}^2$ , and  $d_p$ , have a strong impact on the absolute values of  $\sigma_{pp}^{\text{tot}}$ ,  $\sigma_{pp}^{\text{el}}$ , and  $B_{pp}^{\text{el}}$ , hence, can be roughly fixed based on fixed target data. Moreover, the parameter  $d_p \equiv R_{p(N_{\text{GW}})}^2/R_{p(1)}^2$  (similarly,  $d_\pi$  and  $d_K$  for pions and kaons) controls the differences between various Fock states of the proton and thereby governs the rate of low mass diffraction: the diffractive cross sections (8-10) rise with a decrease of  $d_p$  or vanish for  $d_p = 1$ . It is noteworthy that changing the number of GW states considered,  $N_{\text{GW}}$ , requires a retuning of all the above-discussed parameters.

### 3.2 Extension to low energies

In order to extend our treatment to low energies, below 100 GeV lab., we have to take into consideration secondary Reggeon ( $\rho$ ,  $\omega$ ,  $f$ ,  $A_2$ , where relevant) contributions, in addition to Pomeron exchanges. The hadron-proton scattering amplitude thus becomes

$$A_{hp}(s, t) = 2is \sum_{i,j} C_h^{(i)} C_p^{(j)} \int d^2b e^{i\vec{q}_\perp \vec{b}} \left[ 1 - e^{-\chi_{hp}^{(ij)}(s, b)} \right] + \sum_{\mathbb{R}_i} A_{hp}^{\mathbb{R}_i}(s, t), \quad (18)$$

<sup>2</sup>See also the corresponding discussion in Section 5 and Fig. 6 there.

where  $t \simeq -q_{\perp}^2$  is the squared momentum transfer for the process and the Reggeon exchange amplitude  $A_{hp}^{\mathbb{R}_i}$  is defined as (e.g., [26])

$$A_{hp}^{\mathbb{R}_i}(s, t) = s_0 \gamma_h^{\mathbb{R}_i}(t) \gamma_p^{\mathbb{R}_i}(t) \eta_{\mathbb{R}_i}(t) (s/s_0)^{\alpha_{\mathbb{R}_i}(t)}. \quad (19)$$

Here  $\alpha_{\mathbb{R}_i}(t)$  is the Regge trajectory for  $i$ -th Reggeon,  $\gamma_h^{\mathbb{R}_i}$  is its coupling to hadron  $h$ , and  $\eta_{\mathbb{R}_i}$  is the signature factor,

$$\eta_{\mathbb{R}_i}(t) = -\frac{\sigma_{\mathbb{R}_i} + e^{-i\pi\alpha_{\mathbb{R}_i}(t)}}{\sin[\pi\alpha_{\mathbb{R}_i}(t)]}, \quad (20)$$

with  $\sigma_{\mathbb{R}_i} = \pm 1$ .

A remarkable property of Regge trajectories is their linearity,

$$\alpha_{\mathbb{R}_i}(t) \simeq \alpha_{\mathbb{R}_i}(0) + \alpha'_{\mathbb{R}} t, \quad (21)$$

with  $\alpha'_{\mathbb{R}} \simeq 0.9 \text{ GeV}^{-2}$ . Moreover, there is a considerable exchange degeneracy for the trajectories we are interested in:

$$\alpha_{\rho}(0) \simeq \alpha_{\omega}(0) \simeq \alpha_f(0) \simeq \alpha_{A_2}(0) \equiv \alpha_{\mathbb{R}}, \quad (22)$$

with  $\alpha_{\mathbb{R}} \simeq 0.5$ , which allowed one to develop very successful parametrizations of total cross sections for hadron-proton scattering, considering an exchange of a single effective Reggeon [17].

Indeed, using Eqs. (18-22), we get

$$\sigma_{hp}^{\text{tot}}(s) = \frac{1}{s} \text{Im} A_{hp}(s, 0) = 2 \sum_{i,j} C_h^{(i)} C_p^{(j)} \int d^2b \left[ 1 - e^{-\chi_{hp}^{\mathbb{P}(ij)}(s,b)} \right] + \gamma_{hp}^{\mathbb{R}} (s/s_0)^{\alpha_{\mathbb{R}}-1}, \quad (23)$$

where  $\gamma_{hp}^{\mathbb{R}} \equiv \sum_{\mathbb{R}_i} \gamma_h^{\mathbb{R}_i}(0) \gamma_p^{\mathbb{R}_i}(0)$  corresponds to the product of the residues for the effective Reggeon coupling to hadron  $h$  and the proton.

We shall go further and assume an exponential  $t$ -dependence for the vertex factors  $\gamma_h^{\mathbb{R}_i}(t)$ , using the same Regge slopes  $\lambda_h^{\mathbb{R}}$  for all the considered Reggeons, for a given hadron  $h$ :

$$\gamma_h^{\mathbb{R}_i}(t) = \gamma_h^{\mathbb{R}_i}(0) e^{\lambda_h^{\mathbb{R}} t}. \quad (24)$$

In addition, we take into account that real parts of the amplitudes  $A_{hp}^{\mathbb{R}_i}$  are largely canceled between the different Reggeons, such that  $|\text{Re} A_{hp}(s, t)/\text{Im} A_{hp}(s, t)| \lesssim 0.2$  in the energy range of our interest [34]. This allows us to neglect the real part of  $A_{hp}$  since its contribution to the elastic cross section  $\sigma_{hp}^{\text{el}}$  is at the level of few per cent.

Thus, we finally obtain the scattering amplitude in the impact parameter representation as

$$\begin{aligned} \tilde{A}_{hp}(s, b) &= \frac{1}{8\pi^2 s} \int d^2q_{\perp} e^{-i\vec{q}_{\perp} \vec{b}} A_{hp}(s, -q_{\perp}^2) \\ &= i \sum_{i,j} C_h^{(i)} C_p^{(j)} \left[ 1 - e^{-\chi_{hp}^{\mathbb{P}(ij)}(s,b)} \right] + \frac{i \gamma_{hp}^{\mathbb{R}} (s/s_0)^{\alpha_{\mathbb{R}}-1}}{8\pi \lambda_{hp}^{\mathbb{R}}} e^{-\frac{b^2}{4\lambda_{hp}^{\mathbb{R}}}}, \end{aligned} \quad (25)$$

where  $\lambda_{hp}^{\mathbb{R}} = \lambda_h^{\mathbb{R}} + \lambda_p^{\mathbb{R}} + \alpha'_{\mathbb{R}} \ln(s/s_0)$ . It is noteworthy that, when considering the Good-Walker decomposition of hadron wave functions, we used here the same coupling of the effective Reggeon to all the GW states of a given hadron, thereby neglecting color fluctuation effects in low energy scattering.

The total and elastic cross sections are given by the usual expressions:

$$\sigma_{hp}^{\text{tot}}(s) = 2 \int d^2b \text{Im} \tilde{A}_{hp}(s, b) \quad (26)$$

$$\sigma_{hp}^{\text{el}}(s) = \int d^2b |\tilde{A}_{hp}(s, b)|^2, \quad (27)$$

with  $\sigma_{hp}^{\text{inel}} = \sigma_{hp}^{\text{tot}} - \sigma_{hp}^{\text{el}}$ . In turn, the total and particle production cross sections for hadron-nucleus scattering are given by Eqs. (11-12), with the partial interaction profile  $\Gamma_{hp}^{(ij)}$  being now defined as

$$\Gamma_{hp}^{(ij)}(s, b) = 1 - e^{-\chi_{hp}^{\mathbb{P}(ij)}(s, b)} + \Gamma_{hp}^{\mathbb{R}}(s, b) \quad (28)$$

$$\Gamma_{hp}^{\mathbb{R}}(s, b) = \frac{\gamma_{hp}^{\mathbb{R}}(s/s_0)^{\alpha_{\mathbb{R}}-1}}{8\pi\lambda_{hp}^{\mathbb{R}}} e^{-\frac{b^2}{4\lambda_{hp}^{\mathbb{R}}}}. \quad (29)$$

## 4 Treatment of particle production

### 4.1 Basic scheme

The procedure for modeling secondary hadron production follows the standard logic (see, e.g., [20]), further discussed for the case of hadron-proton interaction. One starts with sampling the impact parameter squared  $b^2$  for the collision: uniformly between 0 and a sufficiently large value  $b_{\text{max}}^2$ , and choosing the GW states  $|i\rangle$  and  $|j\rangle$  of the projectile hadron and of the target proton, respectively. Further, one samples an ‘‘absorptive’’ interaction, with the probability  $w_{\text{abs}}$  defined by the integrand in the right-hand-side (rhs) of Eq. (7), or low mass diffractive processes, the corresponding probabilities being defined by the integrands in the rhs of Eqs. (8-10). If neither takes place, a sampling of the impact parameter and of the GW components of the interacting hadrons is repeated.

For an absorptive interaction, one samples the number of cut Pomerons  $n \geq 1$ : according to the Poisson distribution with the average  $2\chi_{hp}^{\mathbb{P}(ij)}(s, b)$  – see the integrand in the rhs of Eq. (6). Further, one proceeds with the energy-momentum sharing between  $2n$  constituent partons of the projectile hadron, to which strings of color field are attached, and similarly for  $2n$  constituent partons of the target proton. Here for the distribution of the fractions  $x^\pm$  of light cone (LC) momenta ( $E \pm p_z$ ) of constituent partons (string ‘‘ends’’), we use

$$f_h^{\text{LC}}(x_1^\pm, \dots, x_{2n}^\pm) \propto \left[ \prod_{i=1}^{2n-2} (x_i^\pm)^{-\alpha_{\text{sea}}} \right] (x_{2n-1}^\pm)^{-\alpha_{\mathbb{R}}} (x_{2n}^\pm)^{-\alpha_r} \delta\left(1 - \sum_{j=1}^{2n} x_j^\pm\right). \quad (30)$$

Here the exponent  $\alpha_{\text{sea}}$  is used for sea (anti)quarks, considering only light  $u$  and  $d$  (anti)quarks as string ends, while the small  $x$  limit of a valence (anti)quark distribution follows the Regge behavior ( $\propto x_{2n-1}^{-\alpha_{\mathbb{R}}}$ ). Similarly, the LC momentum distribution of the remaining valence parton [(anti)quark for  $h$  being a meson or (anti)diquark for a (anti)baryon] follows the corresponding Regge behavior ( $\propto x_{2n}^{-\alpha_r}$ ) [15, 31]:

$$\alpha_u = \alpha_d = \alpha_{\mathbb{R}} \quad (31)$$

$$\alpha_{ud} = \alpha_{uu} + 1 = 2\alpha_N(0) - \alpha_{\mathbb{R}} \quad (32)$$

$$\alpha_s = \alpha_\phi(0) \quad (33)$$

$$\alpha_{us} = \alpha_{ds} = \alpha_{ud} - \alpha_{\mathbb{R}} + \alpha_\phi(0). \quad (34)$$

Regarding the LC momentum distribution of constituent sea quarks, in principle, it should also be characterized by the Regge behavior ( $\propto x_i^{-\alpha_{\mathbb{R}}}$ ) in the low  $x$  limit [15], i.e.,  $\alpha_{\text{sea}} = \alpha_{\mathbb{R}}$ , which was adopted in the QGSJET(-II) model and will also be used for the default tune of this model (see Section 5). However, generally  $\alpha_{\text{sea}}$  can be treated as an adjustable parameter,  $0.5 \leq \alpha_{\text{sea}} < 1$ , since the energy-momentum sharing between constituent partons is expected to be modified by nonlinear interaction effects. Moreover, since such effects become stronger at higher energies, one may use different  $\alpha_{\text{sea}}$  values for string ends corresponding to soft and semihard Pomerons, namely, using a softer distribution (larger  $\alpha_{\text{sea}}$ ) for the latter. In fact, it is the value of this parameter which grossly defines the predictions for the energy dependence of the inelasticity of hadron-nucleus collisions, having thereby a decisive impact on the predicted EAS maximum depth  $X_{\text{max}}$  [35].

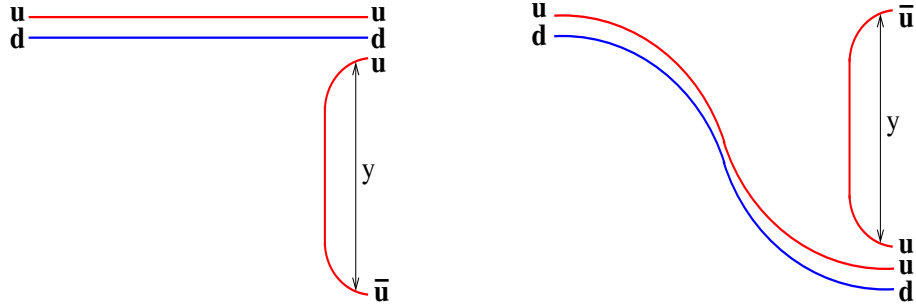


Figure 1: Schematic view of the fragmentation of a fast  $ud$  diquark into a proton: both large  $x$  and small  $x$  limits of the proton LC momentum distribution correspond to a large rapidity  $y$  separation between the  $u$  and  $\bar{u}$  of the vacuum-created  $u\bar{u}$  pair. Left: the large  $x$  limit ( $1-x \propto e^{-y}$ ) is obtained by slowing down the  $\bar{u}$  antiquark. Right: the small  $x$  limit ( $x \propto e^{-y}$ ) corresponds to slowing down both the  $u$  quark and the original  $ud$  diquark.

In turn, transverse momenta of string ends are sampled according to the distribution:

$$f_h^\perp(\vec{p}_{t_1}, \dots, \vec{p}_{t_{2n}}) \propto \exp\left(-\sum_{i=1}^{2n-1} \frac{p_{t_i}^2}{\gamma_\perp} - \frac{p_{t_{2n}}^2}{\gamma_\perp^h}\right) \delta^{(2)}\left(1 - \sum_{j=1}^{2n} \vec{p}_{t_j}\right). \quad (35)$$

The following step is the string fragmentation performed considering iteratively an emission of a hadron from either string end, with the hadron LC momentum fraction  $x$  ( $\text{LC}^+$  or  $\text{LC}^-$  for a projectile or target side end, respectively) and the transverse momentum  $p_t$  in the c.m. frame of the string being sampled according to the distribution:

$$f_{qq' \rightarrow h}^{\text{fragm}}(x, \vec{p}_t) \propto x^{1-\alpha_q-\alpha_{q'}} (1-x)^{\Lambda-\alpha_{q'}} e^{-\frac{p_t}{\gamma_{q'}}}, \quad (36)$$

using Eqs. (31-34) for the relations between the parameters  $\alpha_q$  and the intercepts of the corresponding Regge trajectories. Here the large  $x$  limit is defined by the probability to slow down (move away in rapidity space) the antiparton [(anti)quark or (anti)diquark]  $\bar{q}'$  of the vacuum-created pair, as shown in Fig. 1 (left), while the small  $x$  limit is obtained by slowing down both the original parton  $q$  and the parton  $q'$  attached to it to form the final hadron ( $q + q' \rightarrow h$ ), see Fig. 1 (right) [31]. Various parton-antiparton pairs  $\bar{q}'q'$  created from the vacuum are sampled according to the corresponding probabilities  $a_{q'}$ , relative to  $\bar{u}u$  and  $\bar{d}d$  pairs ( $a_u = a_d = 1/2$ ). The iterative string fragmentation is continued until the mass of the string reminder falls below a specified threshold<sup>3</sup>  $M_{\text{thr}}$ , followed by a modeling of a two particle decay of the remaining string.

The above-discussed treatment takes into account the production of final “stable” hadrons: pions, kaons, nucleons, lambda and sigma baryons, including the corresponding antiparticles, where relevant. Contributions of decays of short-lived resonances are assumed here to be accounted for in the stable hadron yields via the duality principle. The exceptions are the formation of  $\Delta^{++}$  and  $\Delta^-$  resonances (and the corresponding antiparticles) by a fragmentation of constituent  $uu$  and  $dd$  (anti)diquarks as well as the production of  $\rho$  and  $\eta$  mesons, which are also treated explicitly; with the abundance of  $\rho$  mesons, relative to pions, and of  $\eta$ , relative to  $\pi^0$ , being controlled by parameters  $w_\rho$  and  $w_\eta$ , respectively.

In case, a low mass diffractive process is sampled, instead of an absorptive interaction, the mass of a diffractive state  $M_X$  is defined according to the relativistic Breit-Wigner distribution for the corresponding lowest mass resonance ( $N^*$  for nucleons,  $\pi^*$  for pions, and  $K_1$  for kaons),

<sup>3</sup>We use  $M_{\text{thr}}^{qq'} = \sum_{i=1}^3 \sqrt{m_{h_i}^2 + p_{t,\text{thr}}^2}$ , where  $h_1$ ,  $h_2$ , and  $h_3$  correspond to the minimal mass 3-hadron final state for the types  $q$  and  $q'$  of the string end partons.

being matched at half-width to the  $dM_X/M_X^2$  dependence characteristic for the Pomeron-Pomeron-Reggeon (PPR) contribution. The corresponding diffractive final state will consist, respectively, of the products of the resonance decay or of hadrons produced by a fragmentation of a short string, with valence partons of the hadron (e.g., a valence quark and a diquark, for the proton case) “sitting” at the ends of this string. The transverse momentum transfer between the projectile and the target states is modeled as  $\propto dp_t^2 e^{-p_t^2/\gamma_{\text{diff}}}$ , using a fixed<sup>4</sup> parameter  $\gamma_{\text{diff}}$ .

The generalization of the treatment discussed in this Section to the case of hadron-nucleus and nucleus-nucleus collisions is rather straightforward. The only difference to the hadron-proton case is that one considers multi-Pomeron exchanges between the projectile hadron (nucleon) and any of the target nucleons. Correspondingly, multiple strings of color field can be stretched between constituent partons of a given hadron (nucleon) and the ones of a number of different nucleons of the partner nucleus.

## 4.2 Additional improvements

In addition to the basic procedure discussed in Section 4.1, we have a number of modifications of the treatment of absorptive interactions, aimed at improving the description of secondary hadron production in the projectile and target fragmentation regions.

First of all, this concerns the treatment of high mass diffraction (HMD), performed by considering any of the cut Pomerons to be replaced by a diffractive cut of the triple-Pomeron graph corresponding to an interaction between three soft Pomerons, with the probability, for the particular case of projectile hadron HMD,

$$w_{hp(ij)}^{\text{HMD(proj)}}(s, b) = \chi_{hp(ij)}^{\text{HMD(proj)}}(s, b) / \chi_{hp(ij)}^{\mathbb{P}}(s, b). \quad (37)$$

Here the eikonal  $\chi_{hp(ij)}^{\text{HMD(proj)}}$  is defined as

$$\chi_{hp(ij)}^{\text{HMD(proj)}}(s, b) = \frac{G_{\text{PPP}}}{8\pi} \int_{\xi/s}^{s_0/\xi} \frac{dx_{\mathbb{P}}}{x_{\mathbb{P}}} \int d^2b' \chi_{h(i)}^{\mathbb{P}}(x_{\mathbb{P}}s, b') \left( \chi_{p(j)}^{\mathbb{P}}(s_0/x_{\mathbb{P}}, |\vec{b} - \vec{b}'|) \right)^2, \quad (38)$$

where  $G_{\text{PPP}}$  is the triple-Pomeron coupling,  $\xi$  is the minimal mass squared for a Pomeron, and  $\chi_{h(i)}^{\mathbb{P}}$  is the eikonal for a Pomeron exchange between GW state  $|i\rangle$  of hadron  $h$  and the triple-Pomeron vertex.

Using

$$\chi_{h(i)}^{\mathbb{P}}(\hat{s}, b) = \frac{\gamma_{h(i)}(\hat{s}/s_0)^{\Delta_s}}{R_{h(i)}^2 + \alpha'_{\mathbb{P}} \ln(\hat{s}/s_0)} \exp \left[ -\frac{b^2/4}{R_{h(i)}^2 + \alpha'_{\mathbb{P}} \ln(\hat{s}/s_0)} \right], \quad (39)$$

we have

$$\chi_{hp(ij)}^{\text{HMD(proj)}}(s, b) = \frac{G_{\text{PPP}}}{4} \int_{\xi/s}^{s_0/\xi} \frac{dx_{\mathbb{P}}}{x_{\mathbb{P}}^{1+\Delta_s}} \frac{\gamma_{h(i)} \gamma_{p(j)}^2 (s/s_0)^{\Delta_s}}{(R_{p(j)}^2 - \alpha'_{\mathbb{P}} \ln x_{\mathbb{P}})(R_{h(i)}^2 + \frac{1}{2}R_{p(j)}^2 + \alpha'_{\mathbb{P}} \ln(\sqrt{x_{\mathbb{P}}s/s_0}))} \times \exp \left[ -\frac{b^2/4}{R_{h(i)}^2 + \frac{1}{2}R_{p(j)}^2 + \alpha'_{\mathbb{P}} \ln(\sqrt{x_{\mathbb{P}}s/s_0})} \right]. \quad (40)$$

$\chi_{hp(ij)}^{\text{HMD(targ)}}$  for target HMD is obtained interchanging the indexes  $h(i)$  and  $p(j)$  in the rhs of Eq. (40).

In the considered case of projectile diffraction, instead of a pair of strings stretched between constituent partons of the projectile and the target, covering the full available rapidity range for the collision,  $[0, Y]$ ,  $Y = \ln(s/s_0)$ , we have ones covering the rapidity interval  $[Y + \ln x_{\mathbb{P}}, Y]$ , leaving

<sup>4</sup>In principle, the shrinkage of the diffractive cone should lead to some narrowing of the corresponding distribution, i.e., to a decrease of  $\gamma_{\text{diff}}$  with energy. Such an effect is neglected here for simplicity.

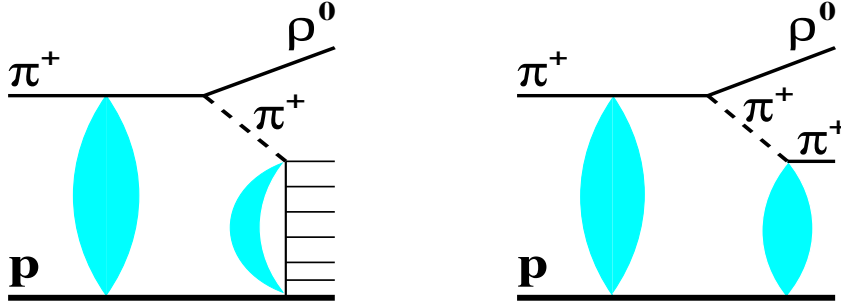


Figure 2: Schematic view of the contributions of absorptive (left) and elastic (right) interactions of the virtual pion to  $\pi^+p$  scattering. The vertical ellipses correspond to the contributions of uncut Pomeron exchanges. In particular, such exchanges between the incoming pion and the proton, shown by the large ellipses, are responsible for absorptive corrections to the processes.

a rapidity gap  $[0, Y + \ln x_{\mathbb{P}}]$  devoid of secondary hadrons. It is noteworthy that we obtain this way a diffractive interaction only in the case when the above-discussed rapidity gap is not covered by secondary hadrons emerging from other inelastic rescattering processes (cut Pomerons). For this to happen, we either should have a single cut Pomeron configuration or, less likely, when all the other cut Pomerons are represented by the same kind of diffractive contribution.

Further, in view of its importance for EAS muon number predictions, one has to take into account  $t$ -channel pion exchange in the Reggeon-Reggeon-Pomeron (RRP) configuration [36]. Here we improve the corresponding treatment of the QGSJET-III model [37], considering explicitly a rescattering of the virtual pion on the partner hadron (nucleus), including the corresponding inelastic and elastic scattering contributions and accounting for impact parameter dependent absorptive corrections for the process (see Fig. 2). In such a case, we have a production of a leading hadron,  $h \xrightarrow{(\pi)} h'$ , and an interaction of the exchanged  $t$ -channel virtual pion with the partner hadron (nucleus), where  $h' = p, n, \Delta^{++}$  for incident proton,  $h' = \rho^\pm, \rho^0$  for incident  $\pi^\pm$ , and  $h' = K^* (\bar{K}^*)$  for incident kaon.

The pion exchange contribution is sampled according to the cross section  $\sigma_{hp}^{\pi\text{-exch}}$  which, for the particular case of virtual pion emission by the projectile hadron, is defined as

$$\sigma_{hp}^{\pi\text{-exch}}(s) = g_{\pi/h} \int d^2b \sum_{i,j} C_h^{(i)} C_p^{(j)} S_{hp}^{(ij)}(s, b) \int dx dt \sum_{h'} f_{h \rightarrow h'}^{(\pi)}(x, t) \Gamma_{\pi p(j)}^{\text{tot}}(\hat{s}_{\pi p}, b). \quad (41)$$

Here  $g_{\pi/h}$  is an adjustable parameter which controls the rate of the process and  $f_{h \rightarrow h'}^{(\pi)}$  corresponds to the distribution of hadron  $h'$ , with respect to the LC momentum fraction  $x$  and the squared momentum transfer  $t$ , in case of an energy-independent interaction of the virtual pion with the target.  $\Gamma_{\pi p(j)}^{\text{tot}}$  is the total (elastic plus inelastic) profile for virtual pion interaction with the target proton represented by its GW state  $|j\rangle$  and  $S_{hp}^{(ij)}$  is the so-called rapidity gap survival factor obtained by considering any number of uncut Pomeron exchanges between the incoming hadron and the target proton (see Fig. 2), represented by GW states  $|i\rangle$  and  $|j\rangle$ , respectively:

$$S_{hp}^{(ij)}(s, b) = e^{-2\chi_{hp}^{\mathbb{P}}(ij)(s, b)}. \quad (42)$$

The interaction profile  $\Gamma_{\pi p(j)}^{\text{tot}}$  is described by (multi)Pomeron exchanges between the virtual pion and the target proton, neglecting Reggeon contributions:

$$\Gamma_{\pi p(j)}^{\text{tot}}(\hat{s}_{\pi p}, b) = 2 \sum_i C_\pi^{(i)} \left[ 1 - e^{-\chi_{\pi p}^{\mathbb{P}}(ij)(\hat{s}_{\pi p}, b)} \right], \quad (43)$$

where the c.m. energy squared  $\hat{s}_{\pi p}$  for the pion-proton interaction is

$$\hat{s}_{\pi p} = (1-x)(s - (m_{h'}^2 + p_t^2)/x). \quad (44)$$

Here the transverse momentum  $p_t$  of the hadron  $h'$  is related to  $t$  as

$$-t = p_t^2/x + (1-x)(m_{h'}^2/x - m_h^2), \quad (45)$$

$m_h$  and  $m_{h'}$  being the masses of  $h$  and  $h'$ , respectively.

The type of hadron  $h'$  as well as its  $x$  and  $p_t$  are sampled according to the product  $f_{h \rightarrow h'}^{(\pi)} \Gamma_{\pi p(j)}^{\text{tot}}$  [cf. the integrand in the rhs of Eq. (41)], with<sup>5</sup> (e.g. [38]):

$$f_{h \rightarrow h'}^{(\pi)}(x, t) = N^{-1} \frac{-t}{(t - m_\pi^2)^2} (1-x)^{1-2\alpha_\pi(t)} e^{b_\pi t}. \quad (46)$$

Here  $N$  is the normalization constant ( $\sum_{h'} \int dx dt f_{h \rightarrow h'}^{(\pi)}(x, t) = 1$ ),  $\alpha_\pi(t) = \alpha'_{\mathbb{R}}(t - m_\pi^2)$  is the pion Regge trajectory,  $m_\pi$  is the pion mass, and we use the same slope  $b_\pi$  for virtual pion emission by any hadron.

With the probability  $\Gamma_{\pi p(j)}^{\text{el}}(\hat{s}_{\pi p}, b)/\Gamma_{\pi p(j)}^{\text{tot}}(\hat{s}_{\pi p}, b)$ , where<sup>6</sup>

$$\Gamma_{\pi p(j)}^{\text{el}}(\hat{s}_{\pi p}, b) = \sum_i C_\pi^{(i)} \left[ 1 - e^{-\chi_{\pi p(ij)}^{\mathbb{P}}(\hat{s}_{\pi p}, b)} \right]^2, \quad (47)$$

we have an elastic scattering of the virtual pion, which simply puts it on shell. Otherwise, we consider an absorptive interaction of the virtual pion, which is modeled as described in Section 4.1. It is noteworthy that absorptive corrections push the pion exchange process towards large impact parameters, with increasing energy. This has two important consequences: i) the energy rise of  $\sigma_{hp}^{\pi\text{-exch}}$  is substantially slowed down, compared to the case when such absorptive corrections are neglected (e.g., [38]); ii) the probability of elastic scattering of the virtual pion decreases with energy.

Finally, regarding nondiffractive production of various hadron species in the projectile and target fragmentation regions, we use a special treatment for the first hadron emission off a string attached to a “remnant” parton [diquark for a nucleon, light (anti)quark for a pion, and strange (anti)quark for a kaon]. Namely, we use the weights for a strange quark-antiquark pair,  $a_{s/h}$ , or for a diquark-antidiquark pair,  $a_{ud/h}$ , where relevant, creation from the vacuum, which differ from the standard string fragmentation parameters  $a_s$  and  $a_{ud}$ , respectively. Phenomenologically, those can be interpreted as being related to “intrinsic strangeness” in nucleons or in pions and “intrinsic baryonic content” of pions or kaons, correspondingly. While a more theoretically consistent approach would be to consider relevant Reggeon exchanges in the  $\mathbb{R}\mathbb{R}\mathbb{P}$  configuration, with  $\mathbb{R} = N, \Delta, K, K^*$ , etc., similarly to the above-described pion exchange treatment, we prefer to use the discussed phenomenological implementation since it is more economic parameter-wise and more intuitively understandable for a potential non-expert model user. Further, in case a single cut Pomeron is attached to a (anti)nucleon, the first hadron emission off a string attached to the “remnant” (anti)diquark is modified, compared to Eqs. (30), (32): replacing the parameter  $\alpha_{qq}$  ( $qq = uu, ud, dd$ , or the corresponding antidiquarks) by  $\alpha_{qq} + \delta$ , using an adjustable parameter  $\delta$ .

### 4.3 Extension to low energies

Moving now to hadron-proton interactions at low energies, with the probability

$$w_{hp}^{\text{inel}(\mathbb{R})}(s) = \sigma_{hp}^{\text{inel}(\mathbb{R})}(s)/\sigma_{hp}^{\text{inel}}(s), \quad (48)$$

<sup>5</sup>In principle, the  $t$ -distribution of Eq. (46) should be modified by absorptive effects caused by the factor  $S_{hp}^{(ij)}(s, b)$  in Eq. (41). Such a modification is neglected here for simplicity.

<sup>6</sup>For simplicity, inelastic diffraction is neglected for virtual pion interactions.

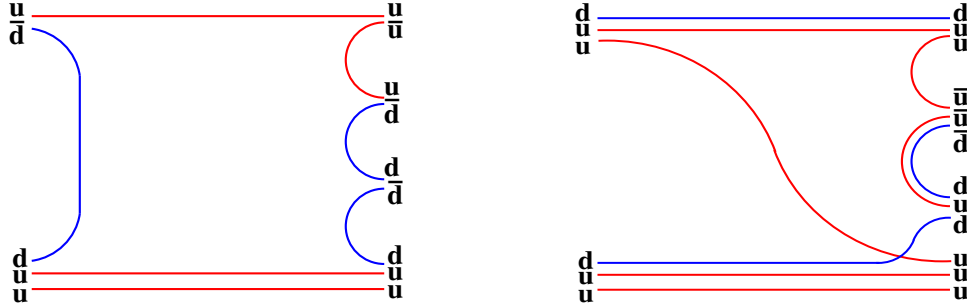


Figure 3: Examples of a planar diagram contribution to hadron production in  $\pi^+p$  scattering (left) and of an undeveloped cylinder diagram contribution to hadron production in  $pp$  scattering (right).

we consider a Reggeon exchange dominated process. Otherwise, particle production is modeled as discussed in Sections 4.1 and 4.2.

Here  $\sigma_{hp}^{\text{inel}(\mathbb{R})}$  is obtained neglecting Pomeron contributions in Eqs. (25-27):

$$\sigma_{hp}^{\text{inel}(\mathbb{R})}(s) = \int d^2b \left[ 2\Gamma_{hp}^{\mathbb{R}}(s, b) - (\Gamma_{hp}^{\mathbb{R}}(s, b))^2 \right] = \gamma_{hp}^{\mathbb{R}}(s/s_0)^{\alpha_{\mathbb{R}}-1} - \frac{[\gamma_{hp}^{\mathbb{R}}(s/s_0)^{\alpha_{\mathbb{R}}-1}]^2}{16\pi\lambda_{hp}^{\mathbb{R}}}. \quad (49)$$

For the Reggeon exchange dominated process, particle production is modeled as a fragmentation of a single string stretched between valence constituents of the interacting hadrons. For  $\bar{p}p$ ,  $\pi^\pm p$ , and  $K^-p$  scattering, we consider the so-called planar diagram exemplified in Fig. 3 (left) for the case of  $\pi^+p$  interaction: an antiquark of the incident hadron [ $\bar{d}$  in Fig. 3 (left)] annihilates with a valence quark of the target proton ( $d$  quark in the Figure), such that a string of color field is formed between the remaining valence parton of the projectile and the target diquark [ $u$  and  $uu$ , respectively, in Fig. 3 (left)]. On the other hand, since such a planar configuration is not possible for  $pp$  and  $K^+p$  scattering, we choose to describe particle production in these reactions by the so-called ‘‘undeveloped cylinder’’ contribution exemplified in Fig. 3 (right) for the case of  $pp$  interaction. In that case, a projectile valence quark [ $u$  quark in Fig. 3 (right)] is combined with a valence diquark ( $uu$  in the Figure) to form a final baryon, while a string of color field is formed between the remaining parton of the projectile (a diquark for incident proton or  $\bar{s}$  for  $K^+$ ) and the target quark.<sup>7</sup> The LC momentum partition between the (here, target) valence quark and the diquark is modeled like in Eq. (30):  $\propto x_{q_v}^{-\alpha_{\mathbb{R}}} x_{qq}^{-\alpha_{qq}} \delta(1 - x_{q_v} - x_{qq})$ .

For hadron-nucleus scattering, we define the probability  $w_{hA}^{\text{prod}(\mathbb{R})}$  as corresponding to configurations of hadron-nucleus collisions, where all inelastic rescattering processes are described by Reggeon exchanges:

$$w_{hA}^{\text{prod}(\mathbb{R})}(s) = \sigma_{hA}^{\text{prod}(\mathbb{R})}(s)/\sigma_{hA}^{\text{prod}}(s), \quad (50)$$

where

$$\begin{aligned} \sigma_{hA}^{\text{prod}(\mathbb{R})}(s) &= \int d^2b \sum_i C_h^{(i)} \left\{ \left[ 1 - \sum_j C_p^{(j)} \int d^2\kappa T_A(\kappa) \right. \right. \\ &\times \left. \left( 1 - e^{-2\chi_{hp}^{\mathbb{P}}(s, |\vec{b}-\vec{\kappa}|)} - 2\Gamma_{hp}^{\mathbb{R}}(s, |\vec{b}-\vec{\kappa}|)(1 - e^{-\chi_{hp}^{\mathbb{P}}(s, |\vec{b}-\vec{\kappa}|)}) \right) \right]^A \\ &- \left. \left[ 1 - \sum_j C_p^{(j)} \int d^2\kappa T_A(\kappa) \left( 1 - e^{-2\chi_{hp}^{\mathbb{P}}(s, |\vec{b}-\vec{\kappa}|)} + \Gamma_{hp}^{\mathbb{R}}(s, |\vec{b}-\vec{\kappa}|) \right) \right] \right\} \end{aligned}$$

<sup>7</sup>For  $pp$  scattering, we consider also the opposite configuration: when a target quark is combined with a projectile diquark and the string is stretched between a projectile quark and a target diquark.

$\Delta_s$	$\Delta_{sh}$	$\alpha'_{\mathbb{P}}$ GeV <sup>-2</sup>	$\delta_{s/sh}$	$g_0$ GeV	$R_{p(1)}^2$ GeV <sup>-2</sup>	$R_{\pi(1)}^2$ GeV <sup>-2</sup>	$R_{K(1)}^2$ GeV <sup>-2</sup>	$d_p$	$d_\pi$	$d_K$
0.06	0.22	0.2	0.92	1.63	2.81	1.32	1.11	0.1	0.17	0.17

Table 1: Model parameters related to Pomeron exchange contributions.

$\alpha_{\mathbb{R}}$	$\alpha'_{\mathbb{R}}$ GeV <sup>-2</sup>	$\gamma_{pp}^{\mathbb{R}}$ GeV <sup>-2</sup>	$\gamma_{\bar{p}p}^{\mathbb{R}}$ GeV <sup>-2</sup>	$\gamma_{\pi^+p}^{\mathbb{R}}$ GeV <sup>-2</sup>	$\gamma_{\pi^-p}^{\mathbb{R}}$ GeV <sup>-2</sup>	$\gamma_{K^+p}^{\mathbb{R}}$ GeV <sup>-2</sup>	$\gamma_{K^-p}^{\mathbb{R}}$ GeV <sup>-2</sup>	$\lambda_p^{\mathbb{R}}$ GeV <sup>-2</sup>	$\lambda_{\bar{p}}^{\mathbb{R}}$ GeV <sup>-2</sup>	$\lambda_{\pi^+}^{\mathbb{R}}$ GeV <sup>-2</sup>	$\lambda_{\pi^-}^{\mathbb{R}}$ GeV <sup>-2</sup>	$\lambda_{K^+}^{\mathbb{R}}$ GeV <sup>-2</sup>	$\lambda_{K^-}^{\mathbb{R}}$ GeV <sup>-2</sup>
0.5	0.9	5.5	11.5	3	4.1	0.8	3	1	3	0	0.4	0	0.4

Table 2: Model parameters related to Reggeon exchange contributions.

$$\times \left( 2e^{-\chi_{hp(ij)}^{\mathbb{P}}(s, |\vec{b}-\vec{\kappa}|)} - \Gamma_{hp}^{\mathbb{R}}(s, |\vec{b}-\vec{\kappa}|) \right) \Big]^A \Big\}, \quad (51)$$

with  $\Gamma_{hp}^{\mathbb{R}}$  being defined in Eq. (29). The corresponding Reggeon exchange dominated particle production is treated in a simplified fashion: as a single hadron-nucleon interaction, i.e., similarly to the hadron-proton case described above.

## 5 Selected results

### 5.1 Hadron-proton and hadron-nucleus cross sections

Using various experimental data on hadron-proton interaction cross sections, we fixed the model parameters describing Pomeron and Reggeon exchanges, considering  $N_{\text{GW}} = 11$  Fock states per hadron, for the GW decomposition of hadron wave functions.<sup>8</sup> The obtained values are compiled in Tables 1 and 2.

The corresponding energy dependence of total and elastic proton-proton and antiproton-proton cross sections is compared to experimental measurements in Fig. 4 (left), while the one for forward elastic proton-proton scattering slope,  $B_{pp}^{\text{el}}$ , is plotted in Fig. 4 (right). The correct description of the latter is also of importance since  $B_{pp}^{\text{el}}$  is proportional to the average impact parameter squared for  $pp$  collisions. Thus, it characterizes the “fatness” of the proton, i.e., the transverse area occupied by its parton “cloud”, which, in turn, impacts the multiple scattering rate in proton-proton and, especially, proton-nucleus (nucleus-nucleus) collisions (see, e.g., the discussion in [41]). Further in Fig. 5, the calculated energy dependence of total and elastic cross sections for pion-proton and kaon-proton scattering is confronted to experimental data. Overall, we have a good description of the experimental data over the wide energy range considered.

In Fig. 6, we plot the energy dependence of inelastic cross sections for  $pp$  and  $\pi^-p$  collisions, showing also partial contributions of Reggeon-dominated interactions [i.e., setting  $\chi_{hp(ij)}^{\mathbb{P}} \equiv 0$  in Eq. (25)], as well as  $\sigma_{pp}^{\text{inel}}$  and  $\sigma_{\pi^-p}^{\text{inel}}$  calculated taking only soft or semihard Pomeron exchange into account. As one can see in the Figure, the Reggeon contribution steeply falls down with energy, becoming insignificant at  $\sqrt{s} \gtrsim 20$  GeV, while the semihard Pomeron starts to dominate the inelastic cross sections at  $\sqrt{s} \gtrsim 2$  TeV.

Further in Fig. 7, we present, as a function of lab. momentum of incident hadron, the calculated total cross sections for proton-carbon and  $\pi^-C$  collisions, as well as particle production cross sections for  $pC$ ,  $\pi^+C$ , and  $K^+C$  interactions. As we can see here, the Glauber-Gribov approach [14, 54] is doing a very good job: using the model parameters tuned to hadron-proton cross section measurements, one obtains a good agreement with hadron-nucleus cross section data.

<sup>8</sup>The model results depend rather weakly on the exact number of GW states considered.

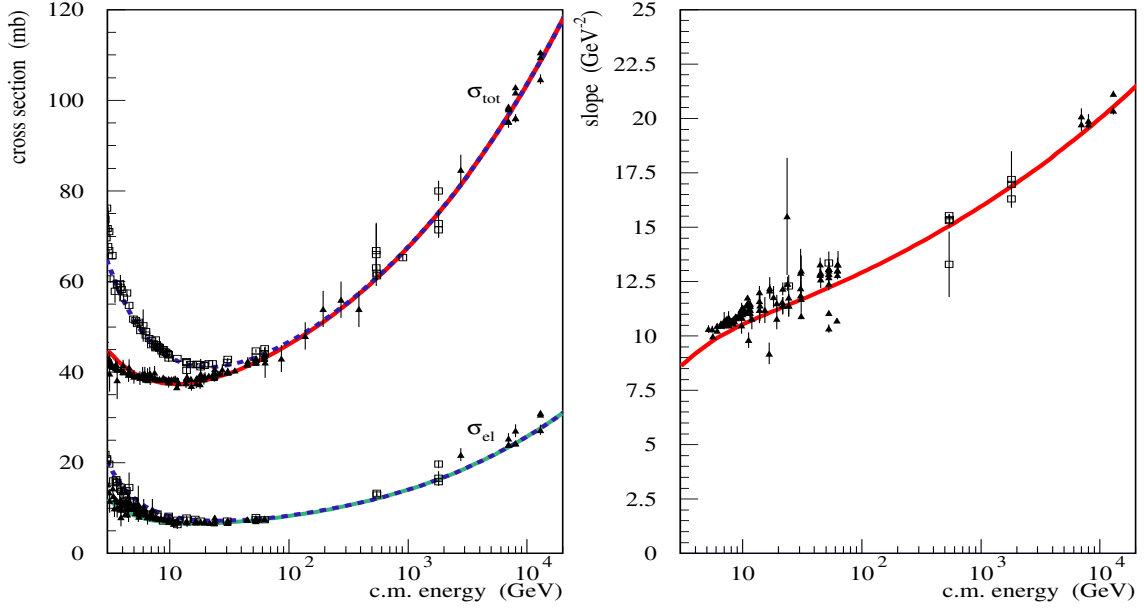


Figure 4: C.m. energy dependence of total and elastic cross sections for  $pp$  and  $\bar{p}p$  scattering (left), and of forward elastic  $pp$  scattering slope (right), compared to experimental data [34, 39, 40] (points):  $pp$  – red solid lines and filled triangles,  $\bar{p}p$  – blue dashed lines and open squares.

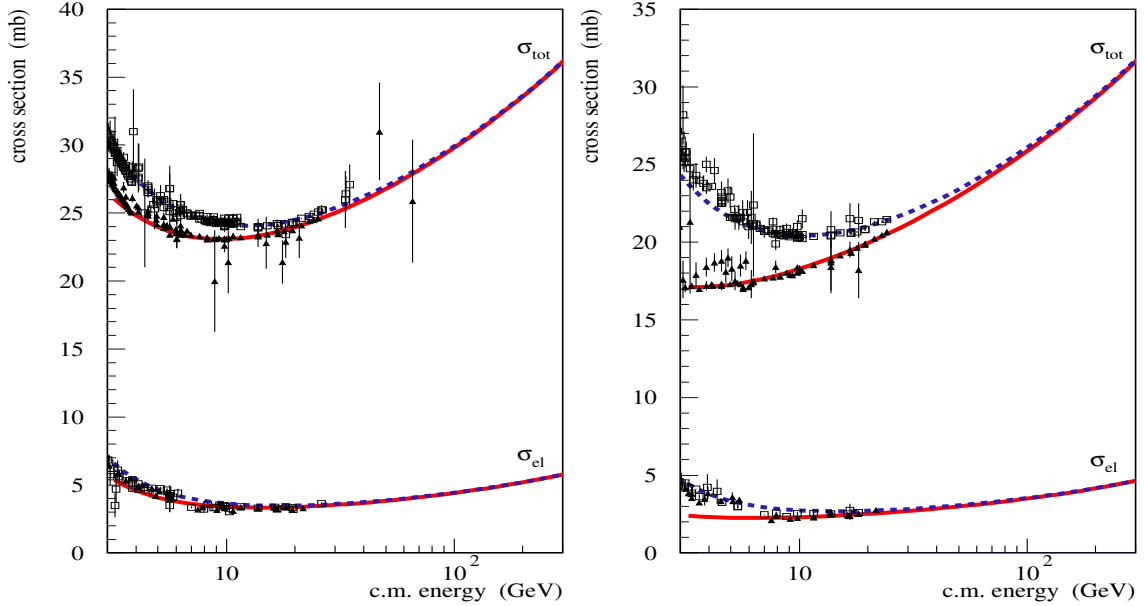


Figure 5: C.m. energy dependence of total and elastic cross sections for pion-proton (left) and kaon-proton (right) scattering, compared to experimental data [34] (points):  $\pi^+p$  and  $K^+p$  – red solid lines and filled triangles;  $\pi^-p$  and  $K^-p$  – blue dashed lines and open squares.

## 5.2 Secondary hadron production

As one can see in Fig. 6, our treatment of hadronic interactions between  $\sqrt{s} \simeq 20$  GeV and  $\sqrt{s} \simeq 1$  TeV is dominated by soft Pomeron exchanges. This allowed us to fix the bulk of hadronization pa-

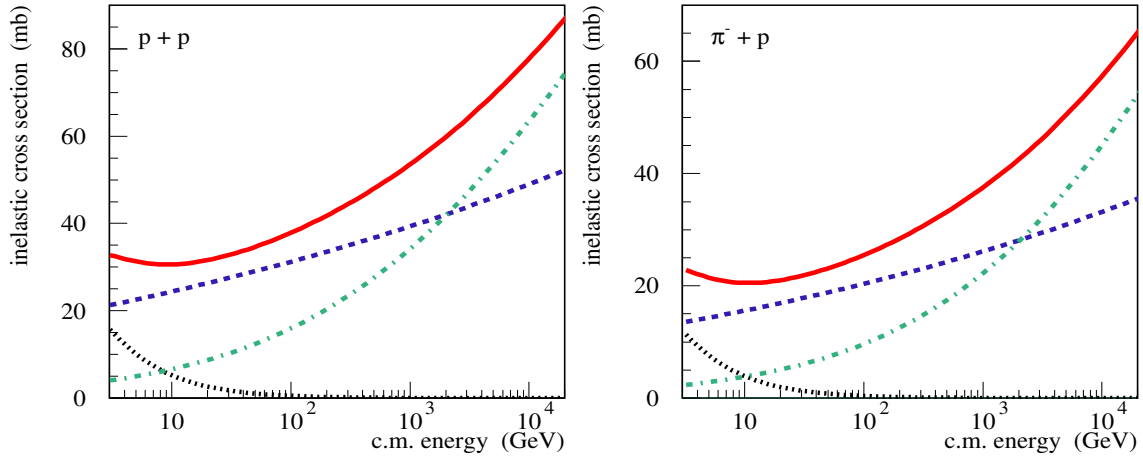


Figure 6: C.m. energy dependence of inelastic  $pp$  (left) and  $\pi^-p$  (right) cross sections – red solid lines. The results for  $\sigma_{pp}^{\text{inel}}$  and  $\sigma_{\pi^-p}^{\text{inel}}$ , obtained by taking into account only Reggeon, soft Pomeron, or semihard Pomeron contributions are plotted by black dotted, blue dashed, and green dash-dotted lines, respectively.

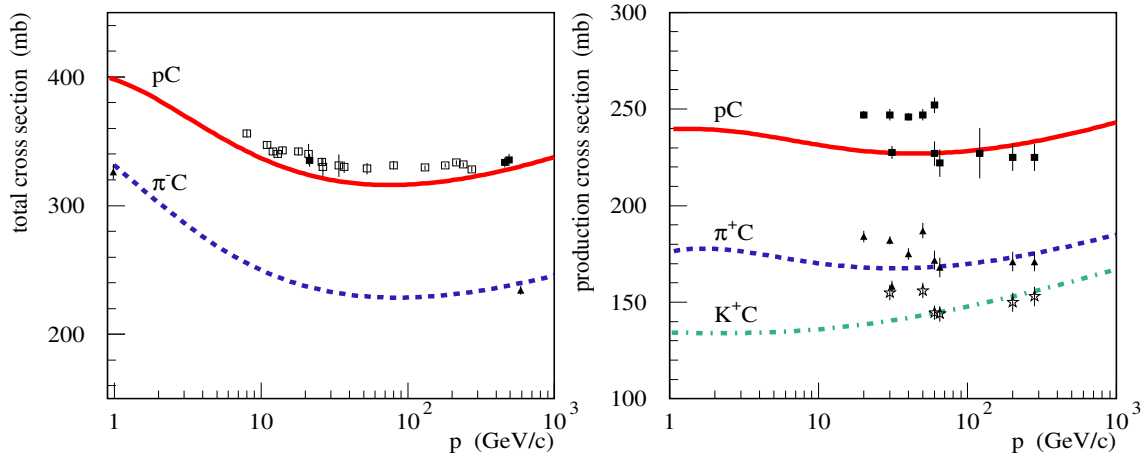


Figure 7: Projectile lab. momentum dependence of total cross sections for  $pC$  and  $\pi^-C$  collisions (left) and of particle production cross sections for  $pC$ ,  $\pi^+C$ , and  $K^+C$  interactions (right), compared to experimental data [42, 43, 44, 45, 46, 47, 48, 49, 50, 51, 52, 53] (points):  $pC$  – red solid lines and filled squares,  $\pi^\pm C$  – blue dashed lines and filled triangles,  $K^+C$  – green dash-dotted line and open stars; data on  $\sigma_{nC}^{\text{tot}}$  – open squares.

parameters of the model, compiled in Tables 3 and 4, using experimental data on hadron production in proton-proton, pion-proton, and kaon-proton collisions in this energy range.

In Fig. 8, we compare our calculations of Feynman  $x$  distributions of secondary hadrons produced in proton-proton interactions, for 158 GeV/c lab. momentum of incident proton, to the corresponding data of the NA49 experiment. As one can see in the Figure, we obtained a good description of the measurements, with the exception of the antiproton spectrum, which is substantially harder than the observed one.

A similar comparison for hadrons produced in proton-carbon collisions, also at 158 GeV/c, is presented in Fig. 9. In contrast to the  $pp$  case in Fig. 8, here we observe a certain excess of protons and neutrons produced at large values of Feynman  $x$ , compared to NA49 data. This may indicate

$\alpha_{\text{sea}}$	$\alpha_N(0)$	$\alpha_\phi(0)$	$\gamma_\perp$	$\gamma_\perp^p$	$\gamma_\perp^\pi$	$\gamma_\perp^K$	$G_{\text{PPP}}$	$\xi$	$\gamma_{\text{diff}}$	$b_\pi$	$g_{\pi/p}$	$g_{\pi/\pi}$	$g_{\pi/K}$
			GeV <sup>2</sup>	GeV <sup>2</sup>	GeV <sup>2</sup>	GeV <sup>2</sup>	GeV	GeV <sup>2</sup>	GeV <sup>2</sup>	GeV <sup>-2</sup>			
0.5	-0.05	0	0.15	0.75	0.2	0.2	0.14	4.5	0.41	0.3	0.15	0.15	0.05

Table 3: Parameters of the hadronization procedure (excluding string fragmentation parameters).

$\Lambda$	$p_{t,\text{thr}}^2$	$a_{ud}$	$a_s$	$a_{us} = a_{ds}$	$a_{s/p}$	$a_{s/\pi}$	$a_{ud/\pi}$	$a_{ud/K}$	$\delta$	$w_\eta$	$w_\rho$	$\gamma_{qq}$	$\gamma_u = \gamma_d$	$\gamma_s$
	GeV <sup>2</sup>											GeV <sup>2</sup>	GeV <sup>2</sup>	GeV <sup>2</sup>
1.7	0.3	0.1	0.1	0.019	0.21	0.19	0.19	0.1	1	0.12	0.4	0.27	0.18	0.24

Table 4: String fragmentation parameters for soft Pomerons.

that the model underestimates somewhat the inelasticity, i.e., the relative energy loss of leading (most energetic) secondary nucleons, in proton-nucleus collisions.

In turn, in Fig. 10, the calculated lab. momentum distributions of various hadrons produced in  $\pi^-$ -C collisions at 158 GeV/c and 350 GeV/c incident pion momenta are compared to measurements by the NA61/SHINE experiment. While our results agree with the observed spectra of charged pions reasonably well, the situation with kaon production is less clear. On the one side, the calculated charged kaon yields are noticeably smaller than the experimental ones. On the other hand, no such “kaon deficiency” is observed for  $K_S^0$ . The NA61/SHINE collaboration interpreted such an enhancement of charged kaon production, relative to neutral kaon yields, as an indication of a substantial violation of the isospin symmetry [61]. However, such a radical assumption may not be necessary, considering a general difficulty to discriminate  $K^\pm$  from abundant charged pions, compared to a more reliable particle identification for  $K_S^0$ . Similar concerns apply to the measured spectra of protons and antiprotons. Tuning the model to the corresponding NA61/SHINE data, as plotted in the bottom row of Fig. 10, we arrive to a substantial overestimation of  $p$  and  $\bar{p}$  yields, compared to results of other experiments (see, e.g., [62] for the corresponding discussion).

Of particular importance are measurements of forward  $\rho^0$  meson production by the NA61/SHINE experiment [63], which allowed us to constrain the rate of the pion exchange process in pion-proton and pion-nucleus collisions by tuning the corresponding parameter  $g_{\pi/\pi}$ . The calculated Feynman  $x$  distributions of  $\rho^0$  mesons, for  $\pi^-$ -C collisions at 158 and 350 GeV/c, are compared to the NA61/SHINE data in Fig. 11. As one can see in the Figure, the contribution of the pion exchange dominates forward  $\rho^0$  meson production, having thereby a strong impact on predictions for muon content of extensive air showers [36].

Also of importance are measurements of secondary proton spectra in the target fragmentation region, in  $pp$ ,  $\pi^+p$ , and  $K^+p$  interactions [64, 65], which allowed us to constrain the rate of low mass diffraction of projectile hadrons. Our calculations are compared in Fig. 12 to the corresponding data for proton-proton collisions at 205 GeV/c, for different selections of momentum transfer squared  $t$  for target proton. In turn, in Fig. 13, the calculated proton spectra in the target fragmentation region in  $\pi^+p$  and  $K^+p$  interactions at 250 GeV/c are compared to the measured ones. As one can see in the Figures, significant contributions to backward proton production come both from low and high mass diffraction of incident hadrons. Moreover, the spectral peak at  $x_F \simeq -1$ , for small values of  $t$ , is dominated by the contribution of the pion exchange process, corresponding to elastic scattering of the virtual pion emitted by the projectile.

Regarding high mass diffraction, the corresponding parameter, the triple-Pomeron coupling  $G_{\text{PPP}}$ , has been fixed based on measured rates of single diffractive-like events in  $pp$  collisions at  $\sqrt{s} = 7$  TeV. The calculated rates are compared in Table 5 to the corresponding data of the TOTEM experiment, for different intervals of mass  $M_X$  of diffractive states produced. Obviously, the agreement between our results and the data is quite good for all  $M_X$  ranges, except the last one corresponding to large  $M_X > 1.15$  TeV.<sup>9</sup>

<sup>9</sup>As discussed in [20], the production of high mass diffractive-like states is dominated by nondiffractive back-

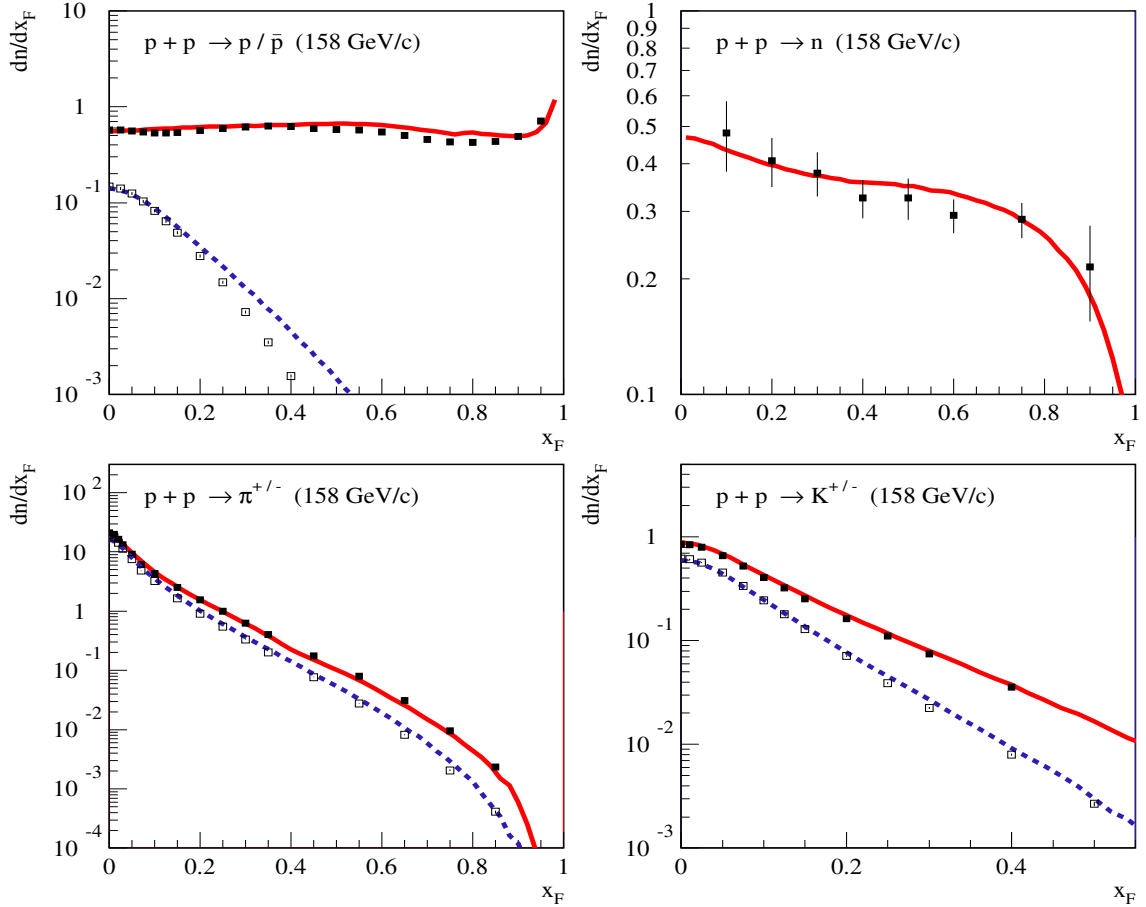


Figure 8: Feynman  $x$  distributions of protons and antiprotons (top left), neutrons (top right), charged pions (bottom left), and charged kaons (bottom right), produced in  $pp$  collisions at 158 GeV/c, compared to NA49 data [55, 56, 57] (points):  $p$ ,  $n$ ,  $\pi^+$ , and  $K^+$  – red solid lines and filled squares;  $\bar{p}$ ,  $\pi^-$  and  $K^-$  – blue dashed lines and open squares.

$M_X$ range, GeV	3.1 – 7.7	7.7 – 380	380 – 1150	1150 – 3100
TOTEM	$1.83 \pm 0.35$	$4.33 \pm 0.61$	$2.10 \pm 0.49$	$2.84 \pm 0.40$
QGSb	1.84	4.37	1.55	5.19

Table 5: Cross sections of single diffractive-like events (in mb), for  $pp$  interactions at  $\sqrt{s} = 7$  TeV, for different ranges of mass  $M_X$  of diffractive states produced, compared to TOTEM data [66].

Moving now to lower energies, where the Reggeon exchange contribution becomes important, we have a reasonable agreement between the calculated rapidity distributions of  $p$ ,  $\bar{p}$ ,  $\pi^\pm$ , and  $K^\pm$ , for  $pp$  interactions at 31, 40, 80, and 158 GeV/c, plotted in Fig. 14, and the corresponding results of the NA61/SHINE experiment. In turn, in Fig. 15, we compare our calculations for lab. momentum distributions of secondary hadrons produced in  $\pi^+C$  collisions at 60 GeV/c, at different polar angles, to the respective data of NA61/SHINE. While the overall agreement with the measurements remains at an acceptable level, we clearly have an excess of charged pion production at small angles,  $\theta \lesssim 20$  mrad, compared to the data.

ground.

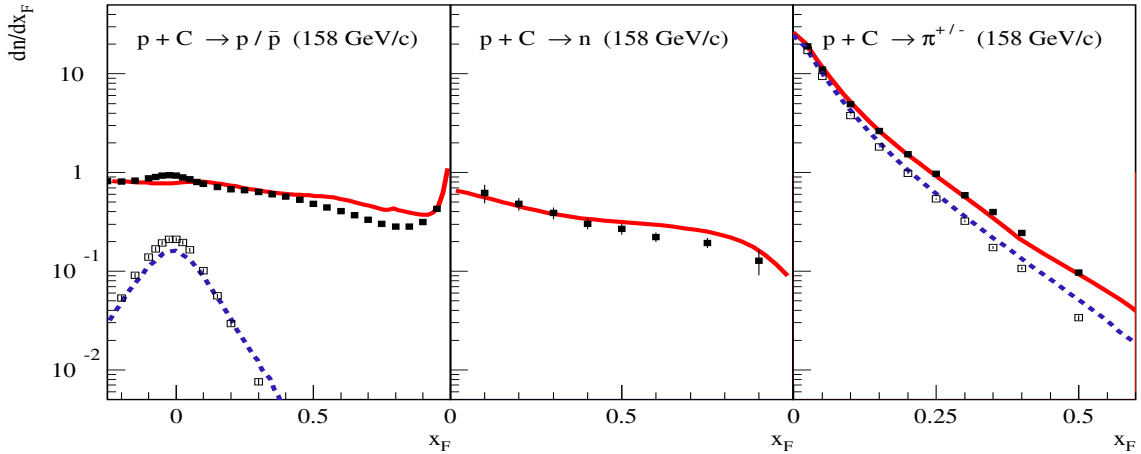


Figure 9: Feynman  $x$  distributions of protons and antiprotons (left panel), neutrons (middle panel), and charged pions (right panel), produced in  $pC$  collisions at 158 GeV/c, compared to NA49 data [58, 59] (points):  $p$ ,  $n$ , and  $\pi^+$  – red solid lines and filled squares;  $\bar{p}$  and  $\pi^-$  – blue dashed lines and open squares.

$\Lambda^{(\text{sh})}$	$a_{ud}^{(\text{sh})}$	$\gamma_{qq}^{(\text{sh})}$ GeV <sup>2</sup>	$\gamma_u^{(\text{sh})} = \gamma_d^{(\text{sh})}$ GeV <sup>2</sup>	$\gamma_s^{(\text{sh})}$ GeV <sup>2</sup>
3.6	0.025	0.45	0.27	0.4

Table 6: String fragmentation parameters for semihard Pomerons, chosen differently from the “soft” fragmentation parameters.

Going to even lower energies, we compare in Figs. 16 and 17 the calculated lab. momentum dependence of inclusive cross sections for charged pion production in  $pC$  and  $\pi^+C$  collisions at 3, 5, 8, and 12 GeV/c, at different polar angles, to the corresponding data of the hadron production (HARP) experiment. Here the model results are again above the measured spectra at small angles, the excess being higher at lower energies and in the target fragmentation region. Nevertheless, the overall description of forward pion production, relevant for EAS modeling, remains reasonable down to very low energies.

Regarding the treatment of very high energy interactions dominated by semihard Pomeron exchanges, one has to take into consideration the changes in the underlying physics. Since the rapid energy rise of the semihard contribution is driven by copious production of hadron (mini)jets, the parameters governing the fragmentation of strings of color field, corresponding to semihard Pomerons, should differ from the ones for soft Pomerons, compiled in Table 4. First of all, as discussed in Section 2, one expects in such a case a higher density of produced hadrons per unit of rapidity, which can be achieved by using a larger value for the parameter  $\Lambda$  [cf. Eq. (36)]. Additionally, the parameters  $\gamma_{qq}$ ,  $\gamma_u$ , and  $\gamma_s$ , which govern the width of transverse momentum distributions of various secondary hadrons, should have larger values. Also the weights for diquark-antidiquark and  $\bar{s}s$  pairs creation from the vacuum may be different from the ones for soft Pomeron strings, reflecting the differences in the kinematics regarding the hadronization of (mini)jets. In Table 6, we compile the parameters for fragmentation of semihard Pomeron strings, which are chosen differently from the “soft” ones specified in Table 4.

In Fig. 18 (left), the calculated pseudorapidity  $\eta$  distributions of charged hadrons,  $dN_{pp}^{\text{ch}}/d\eta$ , with transverse momenta  $p_t > 0.5$  GeV, produced in  $pp$  interactions at  $\sqrt{s} = 0.9, 2.36, 7,$  and 13 TeV, are compared to the corresponding data of the ATLAS experiment, for ATLAS event selection: at least one charged hadron with  $p_t > 0.5$  GeV in the  $|\eta| < 2.5$  range. In turn, in Fig.

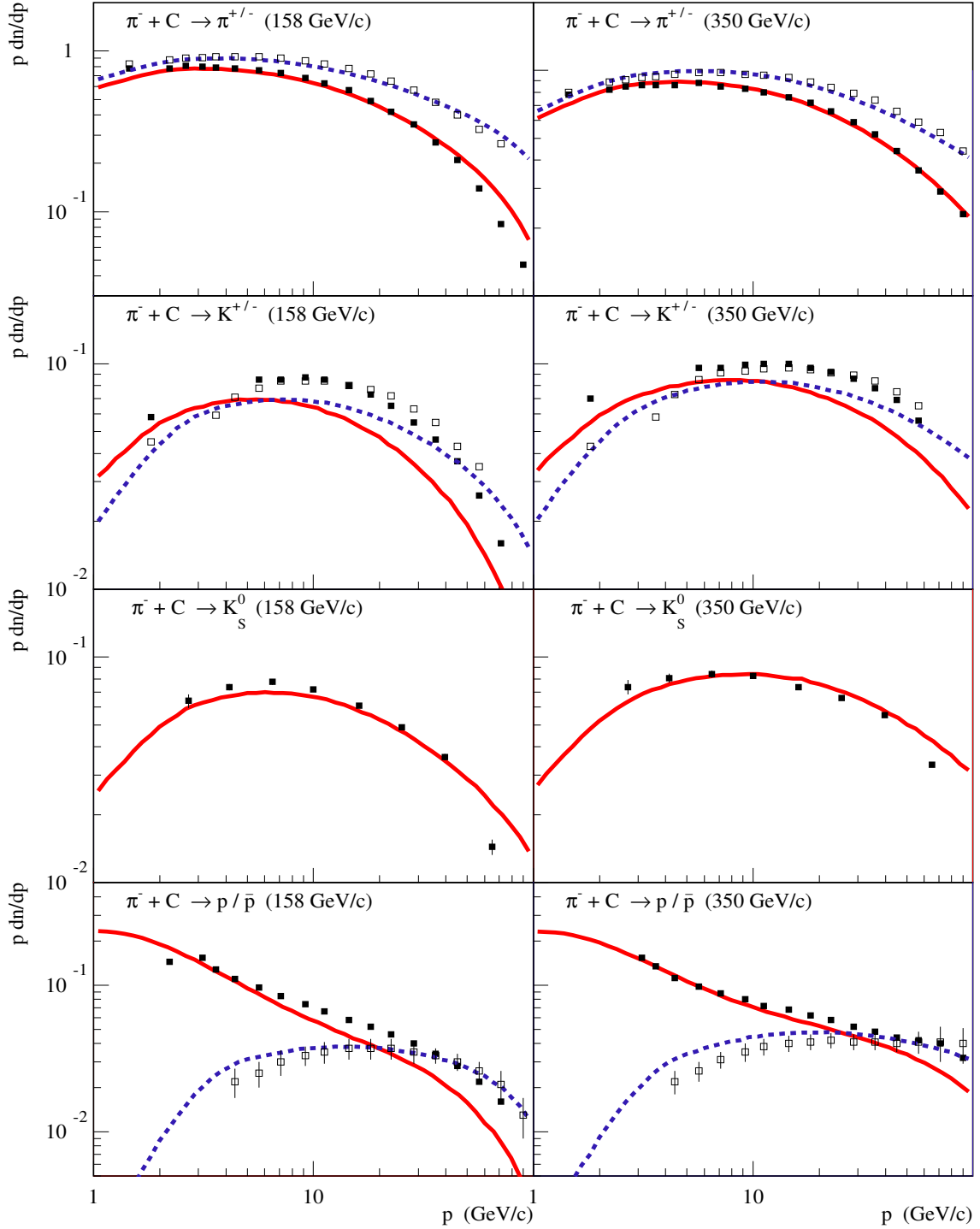


Figure 10: Lab. momentum distributions of, from top to bottom,  $\pi^\pm$ ,  $K^\pm$ ,  $K_S^0$ ,  $p$  and  $\bar{p}$ , produced in  $\pi^-$  C collisions at 158 GeV/c (1st column) and 350 GeV/c (2nd column), compared to NA61/SHINE data [60] (points):  $p$ ,  $\pi^+$ ,  $K^+$ , and  $K_S^0$  – red solid lines and filled squares;  $\pi^-$ ,  $K^-$ , and  $\bar{p}$  – blue dashed lines and open squares.

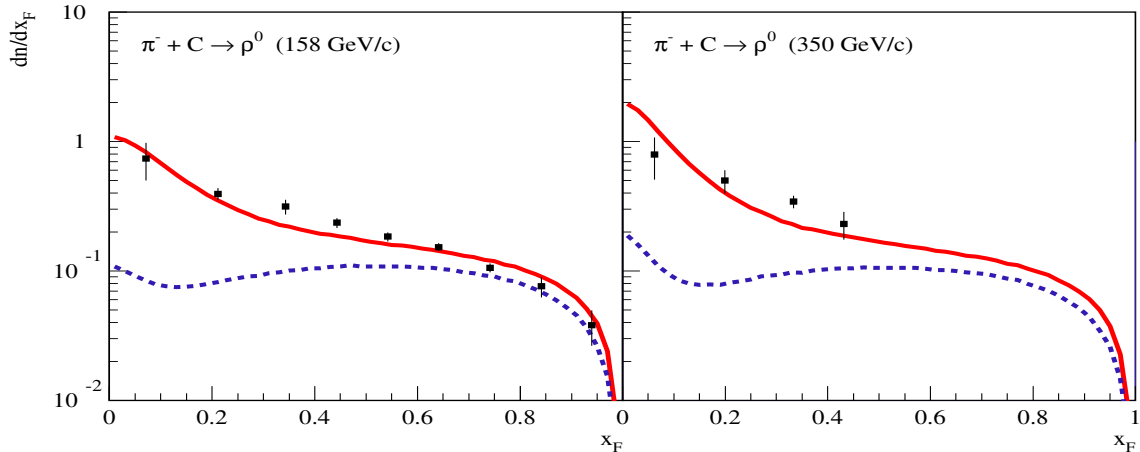


Figure 11: Feynman  $x$  distributions of  $\rho^0$  mesons produced in  $\pi^-$ -C collisions at 158 GeV/c (left) and 350 GeV/c (right) – red solid lines, compared to NA61/SHINE data [63] (points). Shown by blue dashed lines are partial contributions of the pion exchange process, corresponding to virtual pion emission by the incident pion.

18 (right), the corresponding transverse momentum distributions,  $dN_{pp}^{\text{ch}}/dp_t$ , are shown. Overall, we have a reasonable agreement with the measurements for  $dN_{pp}^{\text{ch}}/d\eta$ , over the considered energy range. On the other hand, without an explicit treatment of (mini)jet production, the model clearly fails to describe high  $p_t$  tails of the  $dN_{pp}^{\text{ch}}/dp_t$  distributions.<sup>10</sup>

Regarding model applications to EAS modeling, of major importance is an accurate description of forward particle production in hadronic collisions. In that regard, of particular value are measurements of forward production spectra of neutral pions and neutrons by the LHCf experiment [73, 74], our results being compared to the data in Figs. 19 and 20. As one can see in Fig. 19, we have a good agreement with the measured spectra of neutral pions, for pion energies  $E \lesssim 2$  TeV, corresponding to Feynman  $x_F \lesssim 0.6$ , while predicting harder pion spectra at larger  $x_F$ .<sup>11</sup> Regarding our results for forward neutron spectra, shown in Fig. 20, we have a reasonable overall agreement with the LHCf data. However, somewhat higher neutron yields obtained by us for neutron energies  $E \gtrsim 4$  TeV may indicate that the model underestimates the energy rise of the inelasticity of  $pp$  interactions, which, in turn, may lead to an underestimation of the speed of energy dissipation in hadronic cascades in the atmosphere.

## 6 Predictions for EAS characteristics

The developed model has been implemented in the CONEX EAS simulation program [75] and applied for calculations of basic characteristics of CR-induced extensive air showers. In Fig. 21 (left), our results for the energy dependence of the number of muons  $N_\mu$  at sea level, for muon energy  $E_\mu > 1$  GeV, in vertical proton-initiated EAS, are compared to the corresponding predictions of the EPOS-LHC-R [76], QGSJET-III [20], and QGSJET-II-04 [19] CR interaction models.<sup>12</sup> The values of  $N_\mu$ , obtained with QGSb, are relatively high, approaching at the highest CR energies the

<sup>10</sup>Such high  $p_t$  tails are irrelevant to EAS modeling since very high energy parts of hadronic cascades in the atmosphere are strongly collimated, with hadron production angles in the lab. frame,  $\theta \simeq p_t/E$ , being vanishingly small.

<sup>11</sup>Such high  $x_F$  tails of secondary pion distributions are of minor importance for EAS characteristics [62].

<sup>12</sup>In the corresponding calculations, the QGSb model is used to treat hadronic interactions over the full relevant energy range. On the other hand, the EPOS-LHC-R, QGSJET-III, and QGSJET-II-04 models are applied to describe hadron-air interactions above 80 GeV lab., while employing the UrQMD [77] model at lower energies.

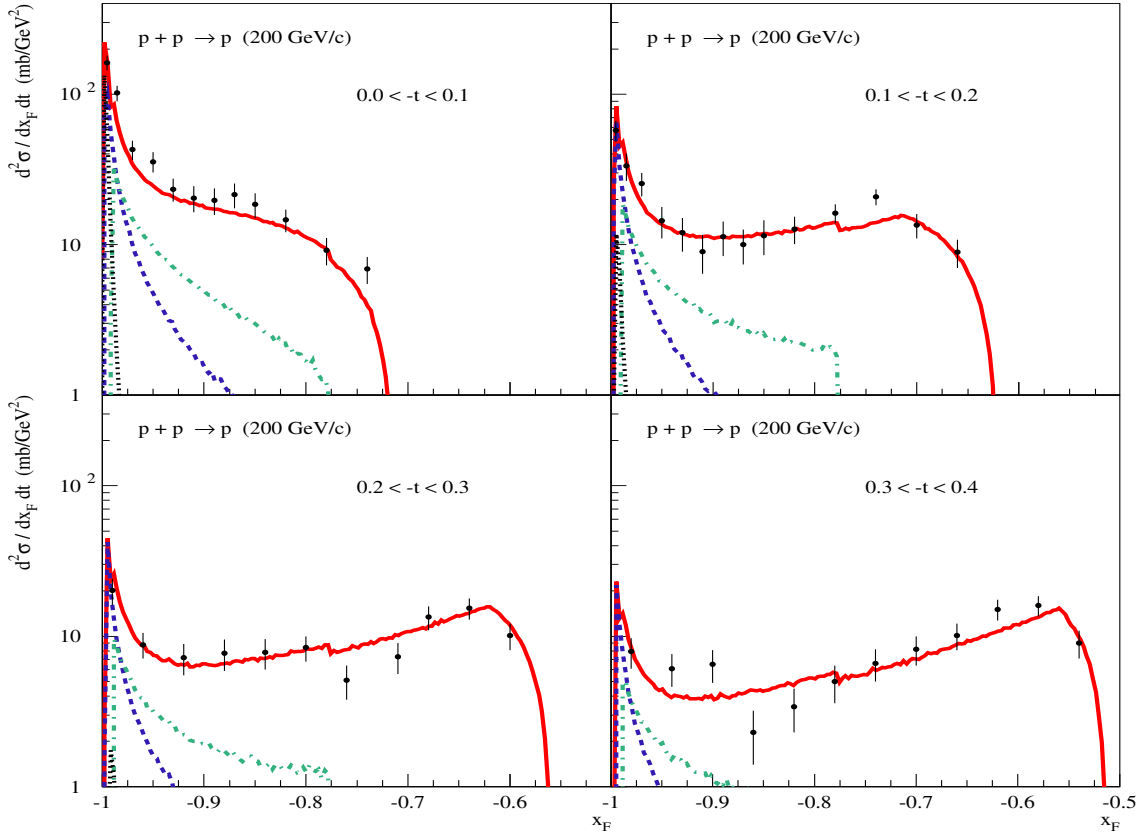


Figure 12: Feynman  $x$  dependence of double differential cross sections,  $d^2\sigma/dx_F/dt$ , for proton production in the target fragmentation region in  $pp$  interactions at 205 GeV/c, for different ranges of  $t$ , as indicated in the plots (red solid lines), compared to experimental data [64] (points). Partial contributions of low and high mass diffraction of incident proton are shown by blue dashed and green dash-dotted lines, respectively, while the contributions of the pion exchange process, corresponding to elastic scattering of the virtual pion emitted by incident proton, are plotted as black dotted lines.

corresponding results of the EPOS-LHC-R MC generator. This is not surprising, given a significant dependence of EAS muon content on forward production of (anti)baryons in pion-air collisions [78] and our calibration to the respective results of the NA61/SHINE experiment, rather than using alternative data sets (see the corresponding discussion in Section 5). In Fig. 21 (right), we compare the energy dependence of  $N_\mu$ , predicted by QGSb, to results of calculations using QGSb in the “standard” high energy range only, above 80 GeV lab., while treating hadron-air interactions at lower energies by means of the FLUKA [79], UrQMD [80], and GHEISHA models. As one can see in the Figure, using the QGSb MC generator for treating the low energy part of extensive air showers gives rise to  $\simeq 5\%$  enhancement of  $N_\mu$ , compared to calculations based on the traditional low energy interaction models. This is again a consequence of the copious (anti)nucleon production in QGSb, which is related to the model calibration to the relevant data of NA61/SHINE.

Further, in Fig. 22, our predictions for EAS maximum depth  $X_{\max}$  and for the corresponding fluctuations are compared to the results of the EPOS-LHC-R, QGSJET-III, and QGSJET-II-04 CR interaction models. Interestingly, at the highest energies, the obtained elongation rate of extensive air showers,  $d \lg X_{\max}(E_0)/dE_0$ , is noticeably smaller, compared to earlier predictions. This is partly related to our treatment of the pion exchange process in proton-proton and proton-nucleus

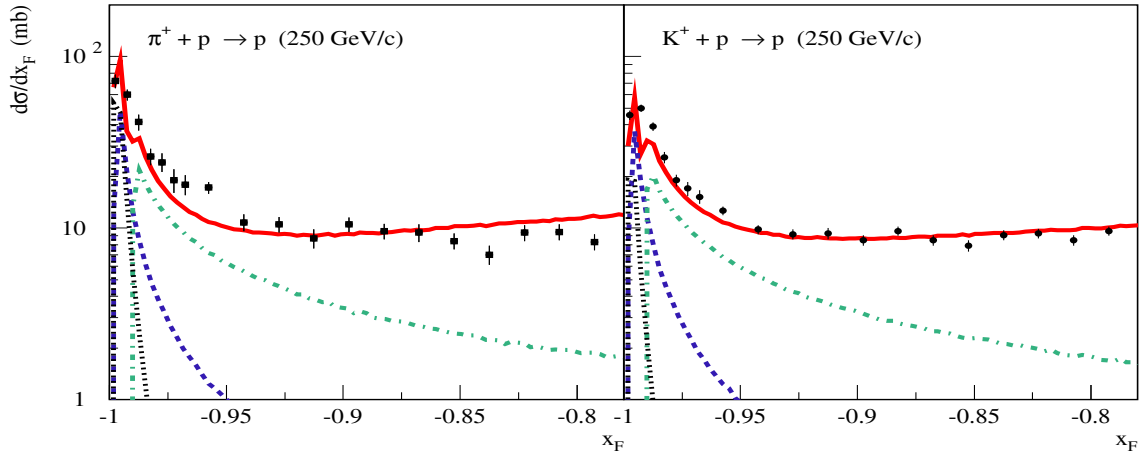


Figure 13: Feynman  $x$  dependence of inclusive cross sections for proton production in the target fragmentation region in  $\pi^+p$  (left) and  $K^+p$  (right) interactions at 250 GeV/c (red solid lines), compared to experimental data [65] (points). Partial contributions of low and high mass diffraction of incident hadrons are shown by blue dashed and green dash-dotted lines, respectively, while the contributions of the pion exchange process, corresponding to elastic scattering of the virtual pion emitted by incident hadrons, are plotted as black dotted lines.

collisions, which takes into consideration the contribution of elastic scattering of virtual pions. As demonstrated in Fig. 12, the process contributes significantly to the peaks in proton spectra at  $|x_F| \simeq 1$  and thereby impacts the calibration of low mass diffraction treatment of the model to the relevant experimental data. With increasing energy, the pion exchange is pushed towards large impact parameters, which leads to a significant suppression of the contribution of elastic scattering of virtual pions, hence, to a noticeable increase of the inelasticity of proton-proton and proton-nucleus collisions. Another reason for a somewhat higher inelasticity of our model is our treatment of Reggeon exchange contributions, which impacts the model calibration at fixed target energies. In proton-proton and proton-nucleus collisions, the “undeveloped cylinder” process exemplified in Fig. 3 (right) contributes noticeably to forward production of nucleons. However, with increasing energy, the process quickly dies out, which leads effectively to an increasing energy loss of leading nucleons. Yet predictions for  $X_{\max}$  depend strongly on model assumptions regarding momentum distributions of constituent partons to which string of color field are attached [35, 81, 82, 83], which is controlled by the  $\alpha_{\text{sea}}$  parameter of the model. Choosing a larger value for  $\alpha_{\text{sea}}$  would shift our predictions for EAS maximum depth deeper in the atmosphere. The corresponding model uncertainty will be studied elsewhere.

Regarding fluctuations of EAS maximum depth, our results for  $\sigma(X_{\max})$ , plotted in Fig. 22 (right), agree with the ones of the other models. This is not surprising, given very precise measurements of total and elastic proton-proton interaction cross sections at the Large Hadron Collider. The spread of the model predictions for  $\sigma(X_{\max})$  can be explained by uncertainties regarding the rate of inelastic diffraction in  $pp$  collisions [84].

Finally, our predictions for maximal muon production depth  $X_{\max}^{\mu}$  are compared to the corresponding results of the other CR interaction models in Fig. 23. As discussed in [85], measurements of this quantity by the Pierre Auger Observatory [8] allow one to substantially constrain both the treatment of pion-air interactions at the highest energies and the corresponding predictions for  $X_{\max}$ . The obtained values of  $X_{\max}^{\mu}$  are between the results of the other models, approaching the ones of the QGSJET-II-04 MC generator at the highest energies. The origin of the latter trend is the same as for  $X_{\max}$  above: being mostly related to the contribution of elastic scattering of virtual pions in the pion exchange process, dying out with energy.

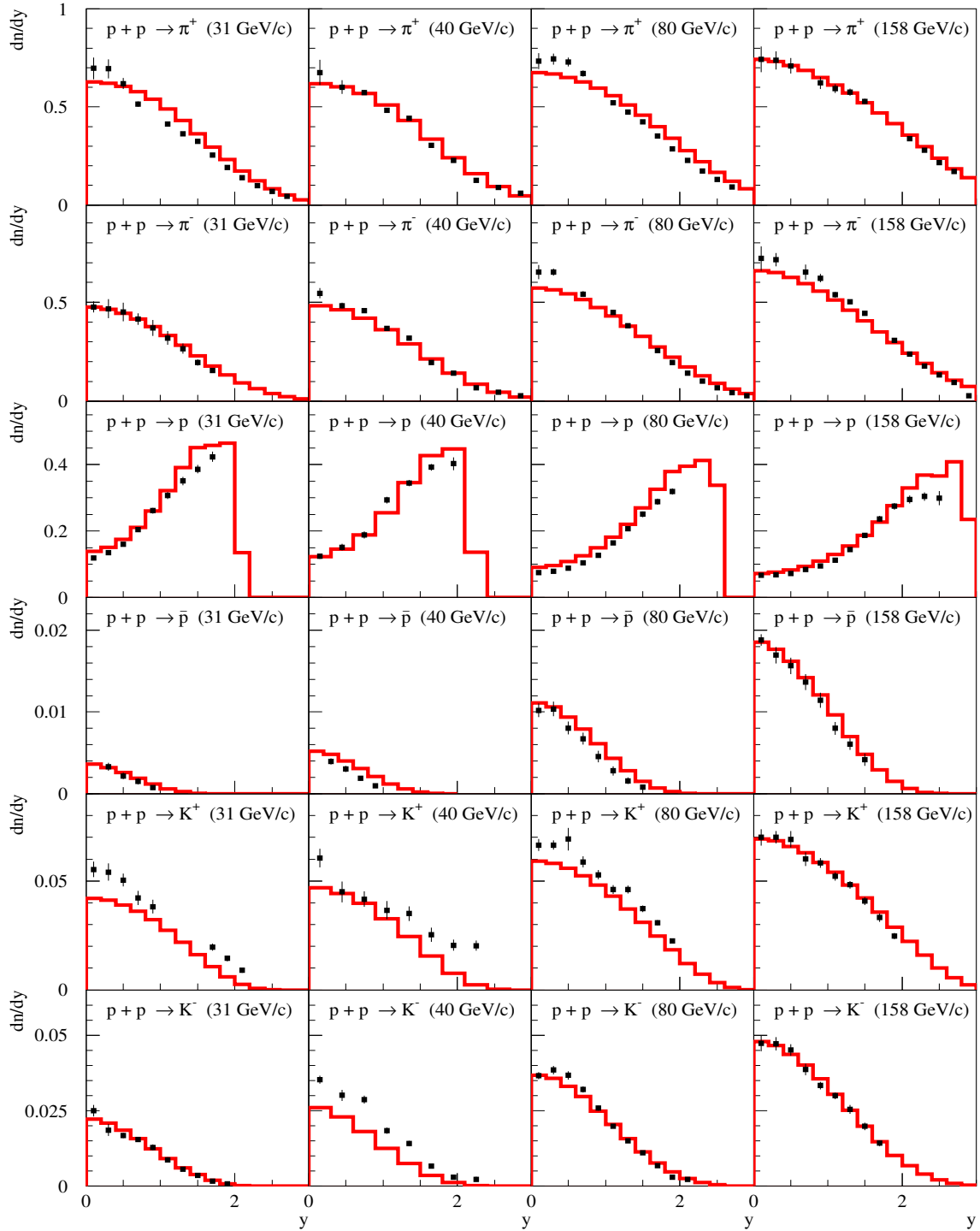


Figure 14: Rapidity distributions (in c.m. frame) of, from top to bottom,  $\pi^+$ ,  $\pi^-$ ,  $p$ ,  $\bar{p}$ ,  $K^+$ , and  $K^-$ , produced in  $pp$  collisions at 31, 40, 80, and 158 GeV/c, as indicated in the plots, compared to NA61/SHINE data [67] (points).

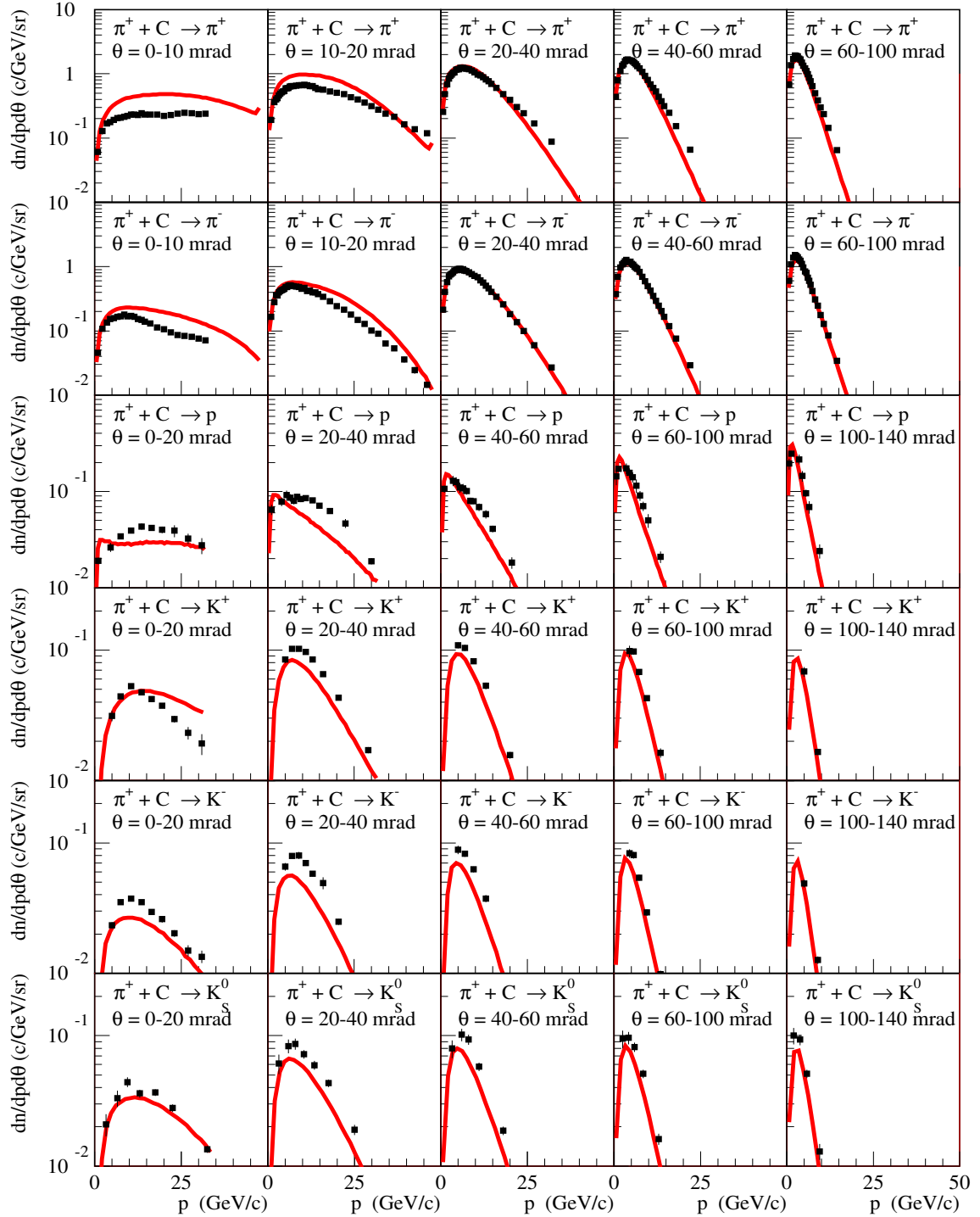


Figure 15: Lab. momentum distributions of, from top to bottom,  $\pi^+$ ,  $\pi^-$ ,  $p$ ,  $K^+$ ,  $K^-$ , and  $K_S^0$ , produced in  $\pi^+C$  collisions at 60 GeV/c, at different polar angles, as indicated in the plots, compared to NA61/SHINE data [68] (points).

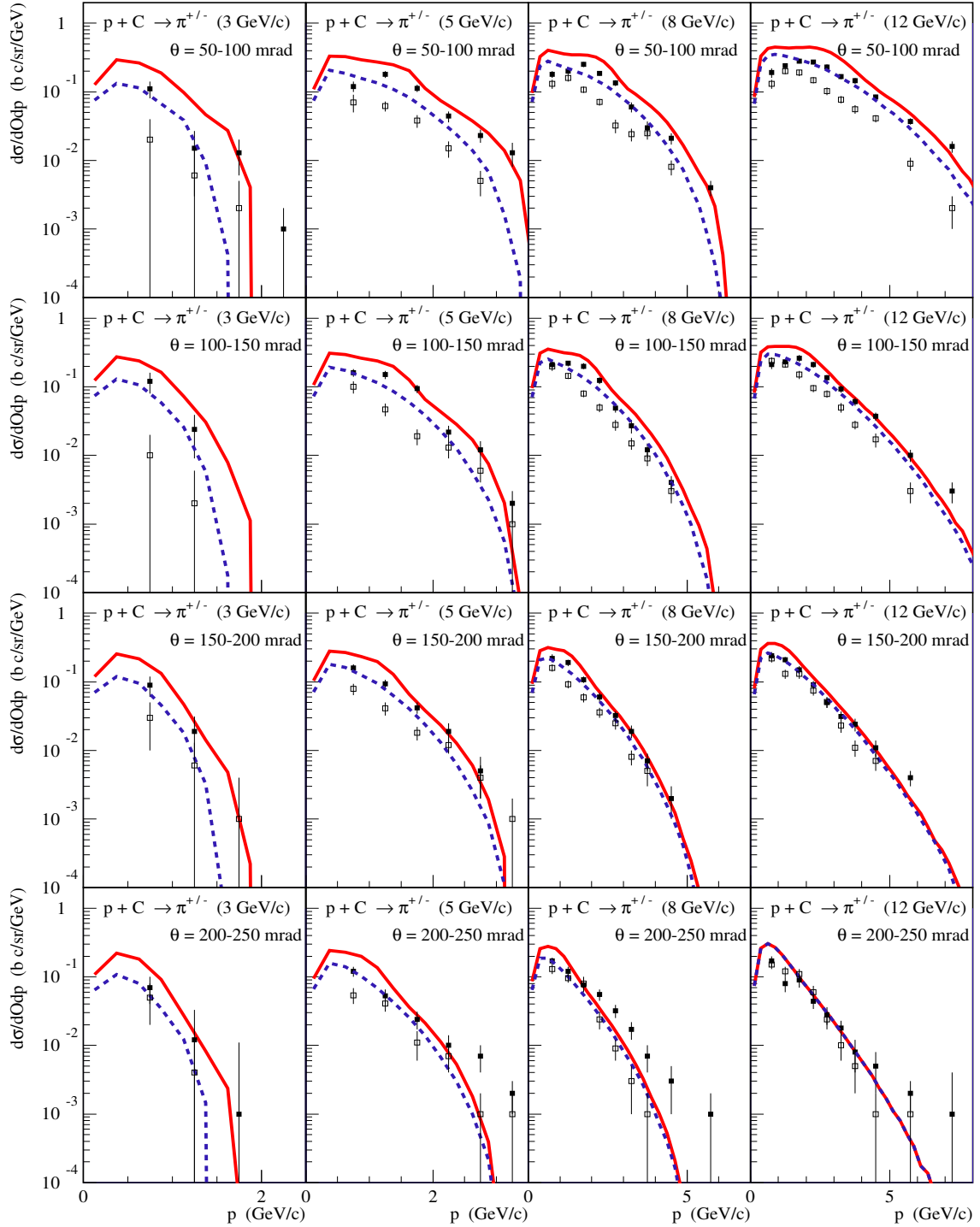


Figure 16: Lab. momentum dependence of inclusive cross sections for charged pion production, at different polar angles, in  $pC$  collisions at 3, 5, 8, and 12 GeV/c, as indicated in the plots, compared to HARP data [69] (points):  $\pi^+$  – red solid lines and filled squares,  $\pi^-$  – blue dashed lines and open squares.

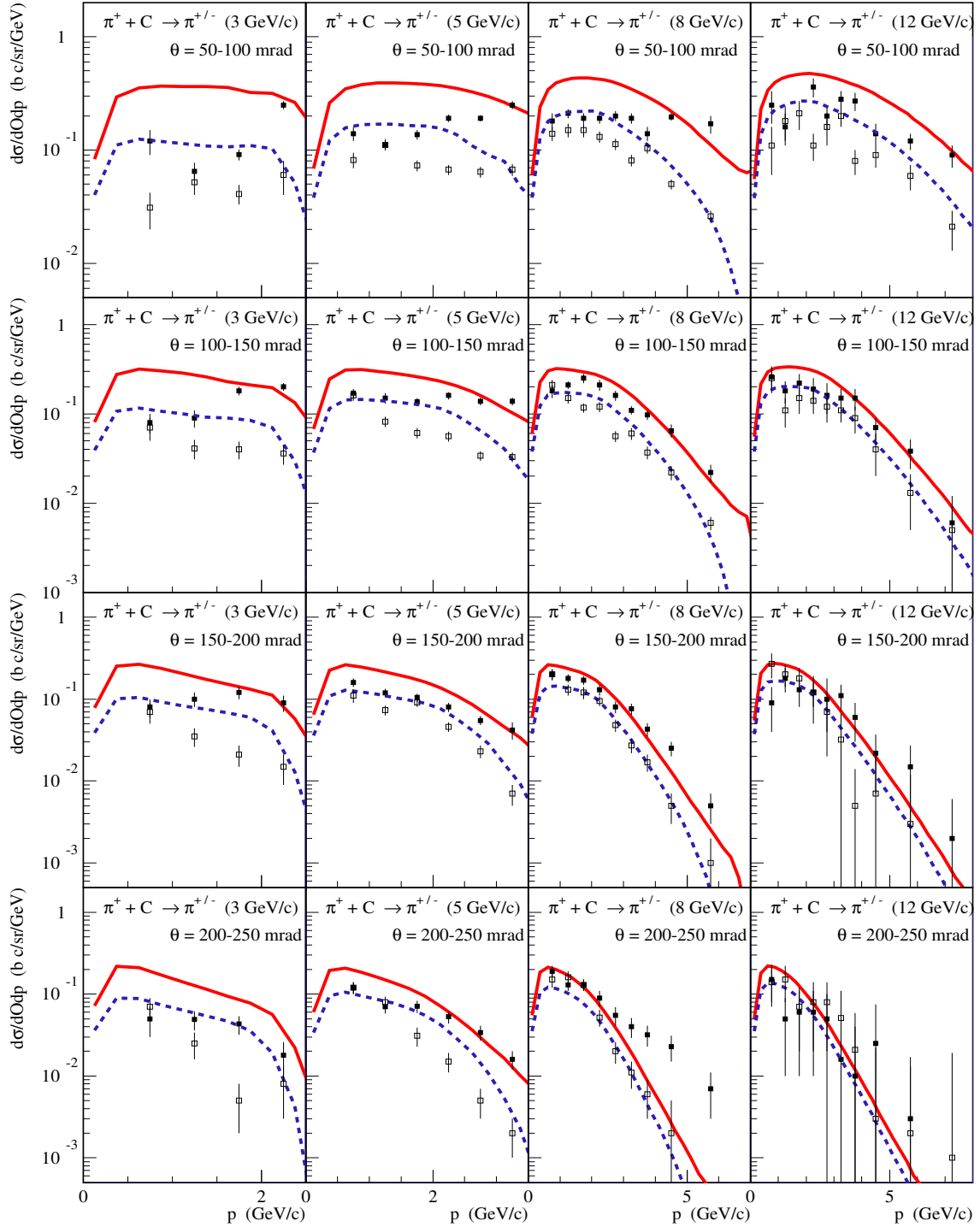


Figure 17: Lab. momentum dependence of inclusive cross sections for charged pion production, at different polar angles, in  $\pi^+C$  collisions at 3, 5, 8, and 12 GeV/c, as indicated in the plots, compared to HARP data [70] (points):  $\pi^+$  – red solid lines and filled squares,  $\pi^-$  – blue dashed lines and open squares.

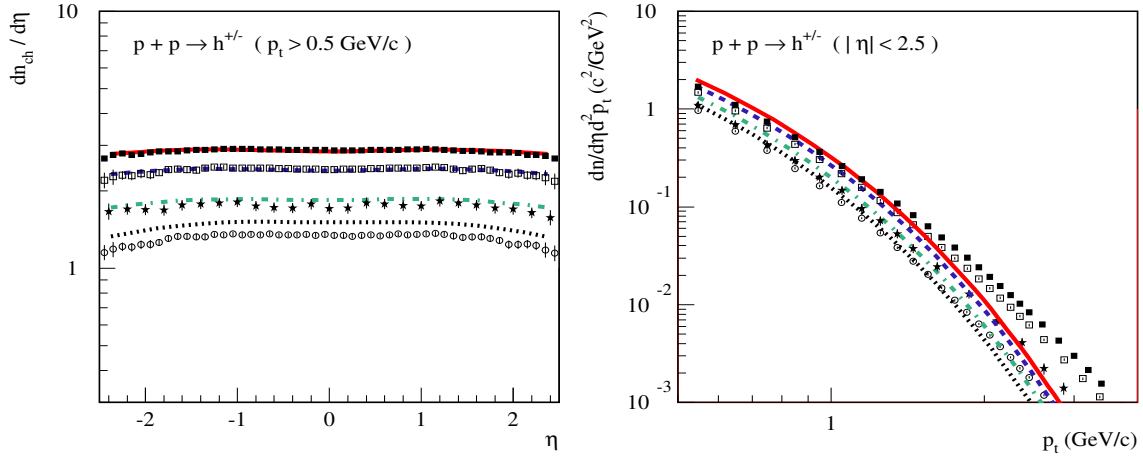


Figure 18: Pseudorapidity (left) and transverse momentum (right) distributions of charged hadrons in c.m. frame, produced in  $pp$  collisions at different  $\sqrt{s}$ , compared to ATLAS data [71, 72] (points):  $\sqrt{s} = 13$  TeV – red solid lines and filled squares;  $\sqrt{s} = 7$  TeV – blue dashed lines and open squares;  $\sqrt{s} = 2.36$  TeV – green dash-dotted lines and filled stars;  $\sqrt{s} = 0.9$  TeV – black dotted lines and open circles.

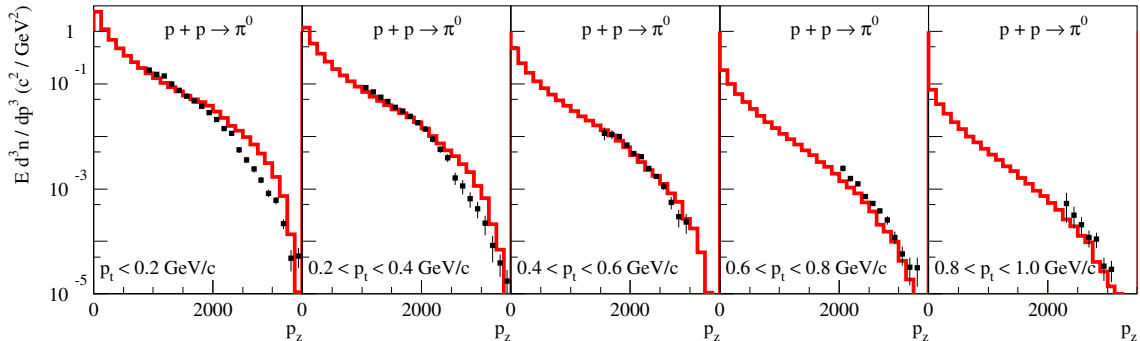


Figure 19: Invariant momentum spectra of neutral pions in c.m. frame,  $E d^3n_{pp}^{\pi^0}/dp^3$ , for  $pp$  collisions at  $\sqrt{s} = 7$  TeV, for different  $p_t$  selections, as indicated in the plots, compared to LHCf data [73] (points).

## 7 Outlook

We developed a new MC generator designed to treat hadronic interactions in a broad energy range: from  $\sim 10$  GeV lab. up to the highest energies of cosmic rays observed. We relied on a relatively simple and transparent interaction picture, while using the theoretical formalism of the Reggeon Field Theory [13, 14]. Basically, we employed the concepts of the original Quark-Gluon String and Dual Parton models [15, 16], describing high energy hadron-proton, hadron-nucleus, and nucleus-nucleus collisions by multi-Pomeron exchanges.

To mimic the transition from soft to semihard physics, regarding the “parton content” of the Pomeron, we considered two contributions to the Pomeron amplitude: the one corresponding to soft parton cascade, characterized by a rather slow energy rise, and the semihard one quickly rising with energy.

Regarding the description of inelastic diffraction, we relied on the traditional Good-Walker approach to treat low mass diffractive excitations of interacting hadrons (nucleons) and the corre-

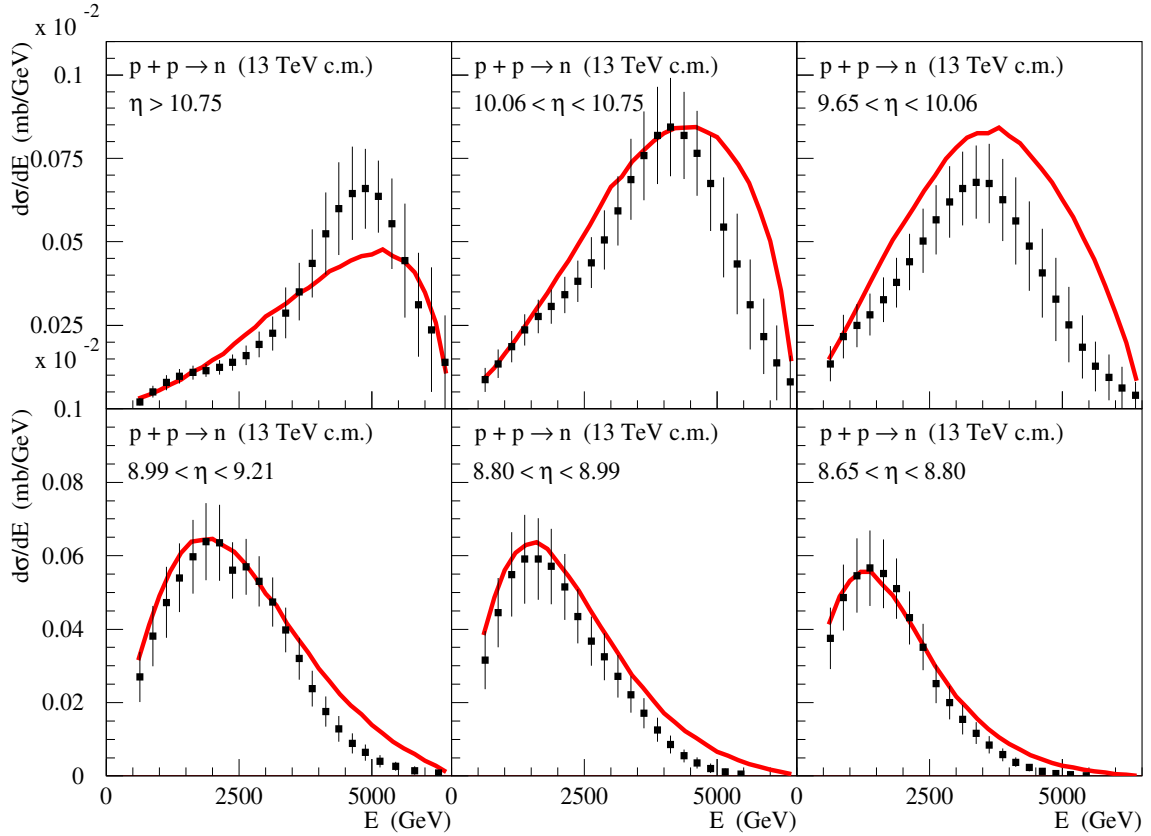


Figure 20: Energy dependence of neutron production spectra in c.m. frame, for  $pp$  collisions at  $\sqrt{s} = 13$  TeV, for different pseudorapidity intervals, as indicated in the plots, in comparison to LHCf data [74] (points).

sponding inelastic screening effects. In turn, for high mass diffraction, we considered the diffractive cut of the simplest triple-Pomeron graph corresponding to an interaction between three soft Pomerons.

In view of its importance for EAS muon number predictions, we took into consideration the  $t$ -channel pion exchange process, improving the respective treatment of the QGSJET-III model. Namely, we considered explicitly a rescattering of virtual pions emitted by interacting hadrons (nucleons), including the corresponding inelastic and elastic scattering contributions and accounting for impact parameter dependent absorptive corrections for the process.

In order to extend the model for a description of hadronic interactions at relatively low energies, below 100 GeV lab., we took into account contributions of secondary Reggeon exchanges, following the approach proposed in [17]: considering an exchange of a single effective Reggeon per reaction type.

The parameters of the model have been tuned based on a variety of accelerator data regarding the energy dependence of total, elastic, and particle production cross sections for hadron-proton and hadron-nucleus collisions, and concerning various characteristics of secondary particle production. Overall, the relatively high parameter freedom of the model allowed us to achieve a satisfactory description of the relevant experimental data over the wide energy range considered.

The developed model has been applied for calculations of basic characteristics of CR-induced extensive air showers: number of muons at ground level, EAS maximum depth and its fluctuations, and maximal muon production depth. The obtained results appeared to be consistent with the

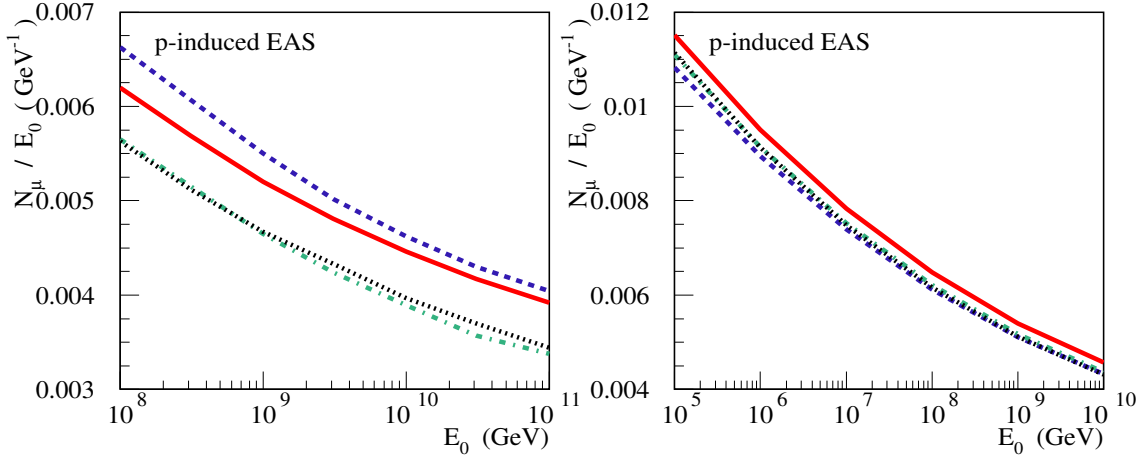


Figure 21: Dependence on primary energy of muon number  $N_\mu$  ( $E_\mu > 1$  GeV) at sea level, for proton-initiated vertical EAS, as calculated using the QGSb model – red solid lines. The corresponding results obtained using the EPOS-LHC-R, QGSJET-III, and QGSJET-II-04 models for treating hadronic interactions above 80 GeV lab., while employing the UrQMD model at lower energies, are shown in the left panel by blue dashed, green dash-dotted, and black dotted lines, respectively. The results obtained using QGSb above 80 GeV lab. and employing the FLUKA, UrQMD, and GHEISHA models at lower energies are shown in the right panel by blue dashed, green dash-dotted, and black dotted lines, respectively.

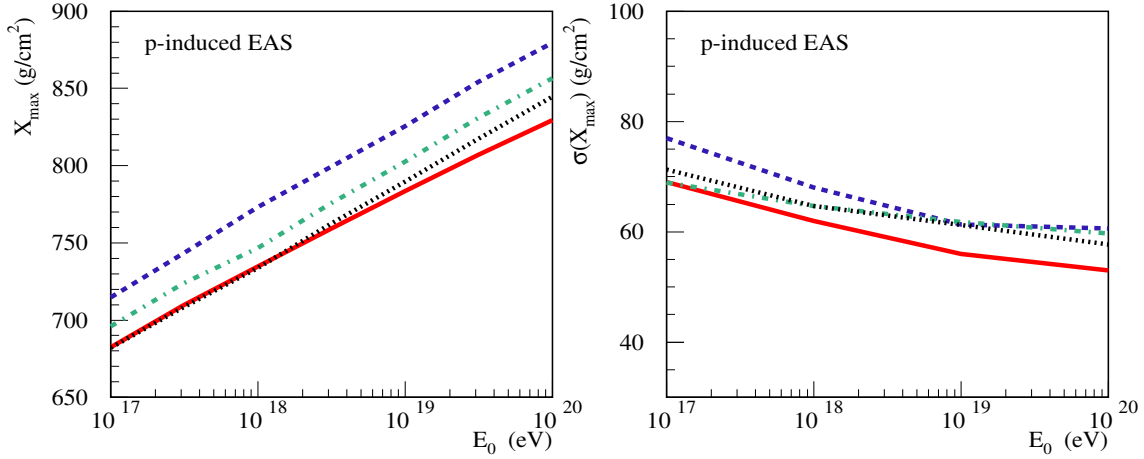


Figure 22: Dependence on primary energy of maximum depth  $X_{\max}$  (left) and of its fluctuations  $\sigma(X_{\max})$  (right), for proton-initiated vertical EAS, as calculated using the QGSb model – red solid lines. Blue dashed, green dash-dotted, and black dotted lines correspond to calculations using the EPOS-LHC-R, QGSJET-III, and QGSJET-II-04 models, respectively, for treating hadronic interactions above 80 GeV lab., while employing the UrQMD model at lower energies.

corresponding predictions of the standard CR interaction models. Yet, at the highest CR energies, the EAS elongation rate predicted by the new model is noticeably smaller, compared to earlier predictions. This stresses the need to consider alternative tunes of the model parameters, allowed by accelerator data, and to study the corresponding uncertainties for EAS predictions. Such an investigation will be reported elsewhere.

One important remark is in order here. The presented model provides an effective description

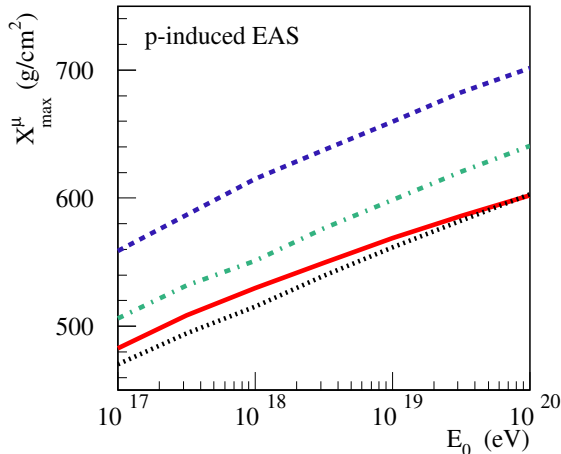


Figure **23**: Dependence on primary energy of maximal muon production depth  $X_{\max}^{\mu}$  ( $E_{\mu} > 1$  GeV), for proton-initiated vertical EAS, as calculated using the QGSb model – red solid line. Blue dashed, green dash-dotted, and black dotted lines correspond to calculations using the EPOS-LHC-R, QGSJET-III, and QGSJET-II-04 models, respectively, for treating hadronic interactions above 80 GeV lab., while employing the UrQMD model at lower energies.

of high energy cosmic ray interactions, addressing the basic physics which is of relevance for calculations of extensive air shower development. However, the latter can potentially be influenced by some other, more specific, interaction mechanisms, e.g., ones discussed in [76, 86], which may be implemented at later stages.

Generally, the developed MC generator can be used both for studying model uncertainties for EAS predictions and for investigating a possibility to describe particular sets of CR data by suitably retuning the model parameters. It is noteworthy that a high computational efficiency of the developed model may allow one to apply automated tuning procedures, e.g., using a combination of accelerator and CR data, as envisaged in [87].

Apart from EAS applications, the developed MC generator can be applied to direct CR studies, e.g., regarding calculations of electron, positron, photon, and (nonprompt) neutrino production in interactions of high energy cosmic rays with the interstellar medium. In that respect, it may complement existing parametrizations of secondary particle spectra for proton-proton and proton-nucleus collisions [88, 89, 90, 91, 92, 93, 94] since the efficiency and transparency of the model can offer here the same advantages as for EAS applications. Namely, potential users of the model may attempt to perform their own tuning of its parameters, either aiming at improving the agreement with particular experimental data sets or investigating the impact of uncertainties regarding the treatment of hadronic interactions on interpretations of various astrophysical data sets.

## Acknowledgments

S.O. acknowledges support from Deutsche Forschungsgemeinschaft (project 550225003). G.S. acknowledges support by the Bundesministerium für Bildung und Forschung, under grant 05A23GU3, and by the Deutsche Forschungsgemeinschaft under Germany’s Excellence Strategy – EXC 2121 “Quantum Universe” – 390833306. This research was supported in part by the Munich Institute for Astro-, Particle and BioPhysics (MIAPbP) which is funded by the Deutsche Forschungsgemeinschaft (DFG, German Research Foundation) under Germany’s Excellence Strategy – EXC-2094 – 390783311. The authors acknowledge useful discussions with T. Sjöstrand and other participants of the 2025 MIAPbP program “Event Generators at Colliders and Beyond Colliders”.

## References

- [1] M. Nagano and A. A. Watson, *Observations and implications of the ultrahigh-energy cosmic rays*, Rev. Mod. Phys. **72**, 689 (2000).
- [2] J. Blümer, R. Engel, and J. R. Hörandel, *Cosmic rays from the knee to the highest energies*, Prog. Part. Nucl. Phys. **63**, 293 (2009).
- [3] R. Engel, D. Heck, and T. Pierog, *Extensive air showers and hadronic interactions at high energy*, Ann. Rev. Nucl. Part. Sci. **61**, 467 (2011).
- [4] T. Pierog, Iu. Karpenko, J. M. Katzy, E. Yatsenko, and K. Werner, *EPOS LHC: Test of collective hadronization with data measured at the CERN Large Hadron Collider*, Phys. Rev. C **92**, 034906 (2015).
- [5] F. Riehn, R. Engel, A. Fedynitch, T. K. Gaisser, and T. Stanev, *Hadronic interaction model Sibyll 2.3d and extensive air showers*, Phys. Rev. D **102**, 063002 (2020).
- [6] S. Ostapchenko, *QGSJET-III model of high energy hadronic interactions: The formalism*, Phys. Rev. D **109**, 034002 (2024).
- [7] P. Abreu et al. (Pierre Auger Collaboration), *Interpretation of the depths of maximum of extensive air showers measured by the Pierre Auger Observatory*, JCAP **02**, 026 (2013).
- [8] A. Aab et al. (Pierre Auger Collaboration), *Muons in air showers at the Pierre Auger Observatory: Measurement of atmospheric production depth*, Phys. Rev. D **90**, 012012 (2014).
- [9] A. Aab et al. (Pierre Auger Collaboration), *Muons in air showers at the Pierre Auger Observatory: Mean number in highly inclined events*, Phys. Rev. D **91**, 032003 (2015).
- [10] A. Aab et al. (Pierre Auger Collaboration), *Testing hadronic interactions at ultrahigh energies with air showers measured by the Pierre Auger Observatory*, Phys. Rev. Lett. **117**, 192001 (2016).
- [11] A. Abdul Halim et al. (Pierre Auger Collaboration), *Testing hadronic-model predictions of depth of maximum of air-shower profiles and ground-particle signals using hybrid data of the Pierre Auger Observatory*, Phys. Rev. D **109**, 102001 (2024).
- [12] J. Ebr, J. Blažek, J. Vicha, T. Pierog, E. Santos, P. Trávníček, N. Denner, and R. Ulrich, *Impact of modified characteristics of hadronic interactions on cosmic-ray observables for proton and nuclear primaries*, PoS **ICRC2023**, 245 (2023).
- [13] V. N. Gribov, *A reggeon diagram technique*, Sov. Phys. JETP **26**, 414 (1968).
- [14] V. N. Gribov, *Glauber corrections and the interaction between high-energy hadrons and nuclei*, Sov. Phys. JETP **29**, 483, (1969).
- [15] A. B. Kaidalov and K. A. Ter-Martirosyan, *Pomeron as quark-gluon strings and multiple hadron production at SPS collider energies*, Phys. Lett. B **117**, 247 (1982).
- [16] A. Capella, U. Sukhatme, C.-I. Tan, and J. Tran Thanh Van, *Dual parton model*, Phys. Rep. **236**, 225 (1994).
- [17] A. Donnachie and P. V. Landshoff, *Total cross-sections*, Phys. Lett. B **296**, 227 (1992).
- [18] N. N. Kalmykov and S. S. Ostapchenko, *The nucleus-nucleus interaction, nuclear fragmentation, and fluctuations of extensive air showers*, Phys. Atom. Nucl. **56**, 346 (1993).

- [19] S. Ostapchenko, *Monte Carlo treatment of hadronic interactions in enhanced pomeron scheme: QGSJET-II model*, Phys. Rev. D **83**, 014018 (2011).
- [20] S. Ostapchenko, *QGSJET-III model of high energy hadronic interactions: II. Particle production and extensive air shower characteristics*, Phys. Rev. D **109**, 094019 (2024).
- [21] L. Gribov, E. Levin, and M. Ryskin, *Semihard processes in QCD*, Phys. Rep. **100**, 1 (1983).
- [22] A. Donnachie and P. V. Landshoff, *Small  $x$ : Two pomerons!*, Phys. Lett. B **437**, 408 (1998).
- [23] S. Ostapchenko, H. J. Drescher, F. M. Liu, T. Pierog, and K. Werner, *Consistent treatment of soft and hard processes in hadronic interactions*, J. Phys. G **28**, 2597 (2002).
- [24] S. Ostapchenko, *On the re-summation of enhanced pomeron diagrams*, Phys. Lett. B **636**, 40 (2006).
- [25] A. B. Kaidalov, L. A. Ponomarev, and K. A. Ter-Martirosyan, *Total cross-sections and diffractive scattering in a theory of interacting pomerons with  $\alpha_P(0) > 1$* , Sov. J. Nucl. Phys. **44**, 468 (1986).
- [26] P. D. B. Collins, *An introduction to Regge theory and high energy physics*, Cambridge U.P., 1977.
- [27] L. Frankfurt, M. Strikman, D. Treleani, and C. Weiss, *Evidence for color fluctuations in the nucleon in high-energy scattering*, Phys. Rev. Lett. **101**, 202003 (2008).
- [28] M. L. Good and W. D. Walker, *Diffraction dissociation of beam particles*, Phys. Rev. **120**, 1857 (1960).
- [29] S. Ostapchenko, *Total and diffractive cross sections in enhanced pomeron scheme*, Phys. Rev. D **81**, 114028 (2010).
- [30] V. A. Abramovsky, V. N. Gribov, and O. V. Kancheli, *Character of inclusive spectra and fluctuations produced in inelastic processes by multi-pomeron exchange*, Sov. J. Nucl. Phys. **18**, 308 (1974).
- [31] A. B. Kaidalov, *Quark and diquark fragmentation functions in the model of quark gluon strings*, Sov. J. Nucl. Phys. **45**, 902 (1987).
- [32] J. Engel, T. K. Gaisser, T. Stanev, and P. Lipari, *Nucleus-nucleus collisions and interpretation of cosmic ray cascades*, Phys. Rev. D **46**, 5013 (1992).
- [33] V. R. Zoller, *Diffractive scattering off nuclei in the multiple scattering theory with inelastic screening*, Sov. J. Nucl. Phys. **48**, 361(1988).
- [34] R. L. Workman *et al.* (Particle Data Group), *Review of Particle Physics*, Prog. Theor. Exp. Phys. **2022**, 083C01 (2022).
- [35] S. Ostapchenko and G. Sigl, *Model uncertainties for the predicted maximum depth of extensive air showers*, Phys. Rev. D **110**, 063041 (2024).
- [36] S. Ostapchenko, *QGSJET-II: physics, recent improvements, and results for air showers*, EPJ Web Conf. **52**, 02001 (2013).
- [37] S. Ostapchenko, *QGSJET-III model: novel features*, Phys. At. Nucl. **44**, 1017 (2021).
- [38] A. B. Kaidalov, V. A. Khoze, A. D. Martin, and M. G. Ryskin, *Leading neutron spectra*, Eur. Phys. J. C **47**, 385 (2006).

- [39] G. Antchev et al. (TOTEM Collaboration), *First measurement of elastic, inelastic and total cross-section at  $\sqrt{s} = 13$  TeV by TOTEM and overview of cross-section data at LHC energies*, Eur. Phys. J. C **79**, 103 (2019).
- [40] G. Aad et al. (ATLAS Collaboration), *Measurement of the total cross section and  $\rho$ -parameter from elastic scattering in  $pp$  collisions at  $\sqrt{s} = 13$  TeV with the ATLAS detector*, Eur. Phys. J. C **83**, 441 (2023).
- [41] S. Ostapchenko and M. Bleicher, *Taming the energy rise of the total proton-proton cross-section*, Universe **5**, 106 (2019).
- [42] G. Bellettini, G. Cocconi, A. N. Diddens, E. Lillethun, G. Matthiae, J. P. Scanlon, and A. M. Wetherell, *Proton-nuclei cross sections at 20 GeV*, Nucl. Phys. **79**, 609 (1966).
- [43] J. Engler et al., *Neutron-nucleus total cross-sections between 8 GeV/c and 21 GeV/c*, Phys. Lett. B **32**, 716 (1970).
- [44] L. W. Jones, M. J. Longo, T. P. McCorriston, E. F. Parker, S. T. Powell, and M. N. Kreisler, *Neutron total cross-sections on protons and nuclei in the 10 to 30 GeV/c momentum range*, Phys. Lett. B **36**, 509 (1971).
- [45] S. P. Denisov, S. V. Donskov, Yu. P. Gorin, R. N. Krasnokutsky, A. I. Petrukhin, Yu. D. Prokoshkin, and D. A. Stoyanova, *Absorption cross-sections for pions, kaons, protons and anti-protons on complex nuclei in the 6 to 60 GeV/c momentum range*, Nucl. Phys. B **61**, 62 (1973).
- [46] A. Babaev et al., *Total cross-section measurement of neutrons on protons and nuclei over the energy range 28–54 GeV*, Phys. Lett. B **51**, 501 (1974).
- [47] A. S. Clough et al., *Pion-nucleus total cross-sections from 88 to 860 MeV*, Nucl. Phys. B **76**, 15 (1974).
- [48] P. V. R. Murthy, C. A. Ayre, H. R. Gustafson, L. W. Jones, and M. J. Longo, *Neutron total cross sections on nuclei at Fermilab energies*, Nucl. Phys. B **92**, 269 (1975).
- [49] A. S. Carroll et al., *Total cross-Sections of  $\pi^\pm$ ,  $K^\pm$ ,  $p$  and  $\bar{p}$  on protons and deuterons between 200 GeV/c and 370 GeV/c*, Phys. Lett. B **80**, 423 (1979).
- [50] U. Dersch et al. (SELEX Collaboration), *Total cross-section measurements with  $\pi^-$ ,  $\Sigma^-$  and protons on nuclei around 600 GeV/c*, Nucl. Phys. B **579**, 277 (2000).
- [51] A. Aduszkiewicz et al. (NA61/SHINE Collaboration), *Measurements of total production cross sections for  $\pi^+ + C$ ,  $\pi^+ + Al$ ,  $K^+ + C$ , and  $K^+ + Al$  at 60 GeV/c and  $\pi^+ + C$  and  $\pi^+ + Al$  at 31 GeV/c*, Phys. Rev. D **98**, 052001 (2018).
- [52] A. Aduszkiewicz et al. (NA61/SHINE Collaboration), *Measurements of production and inelastic cross sections for  $p + C$ ,  $p + Be$ , and  $p + Al$  at 60 GeV/c and  $p + C$  and  $p + Be$  at 120 GeV/c*, Phys. Rev. D **100**, 112001 (2019).
- [53] A. Acharya et al. (NA61/SHINE Collaboration), *Measurement of the production cross section of 31 GeV/c protons on carbon via beam attenuation in a 90-cm-long target*, Phys. Rev. D **103**, 012006 (2021).
- [54] R. J. Glauber, *High-energy collision theory*, In: Lectures in theoretical physics, ed. by W. E. Brittin and L. G. Dunham, Interscience Publishers (New York, 1959), vol. 1, pp. 315-414.

- [55] C. Alt *et al.* (NA49 Collaboration), *Inclusive production of charged pions in p+p collisions at 158 GeV/c beam momentum*, Eur. Phys. J. C **45**, 343 (2006).
- [56] T. Anticic *et al.* (NA49 Collaboration), *Inclusive production of protons, anti-protons and neutrons in p+p collisions at 158-GeV/c beam momentum*, Eur. Phys. J. C **65**, 9 (2010).
- [57] T. Anticic *et al.* (NA49 Collaboration), *Inclusive production of charged kaons in p+p collisions at 158 GeV/c beam momentum and a new evaluation of the energy dependence of kaon production up to collider energies*, Eur. Phys. J. C **68**, 1 (2010).
- [58] C. Alt *et al.* (NA49 Collaboration), *Inclusive production of charged pions in p+C collisions at 158 GeV/c beam momentum*, Eur. Phys. J. C **49**, 897 (2007).
- [59] B. Baatar *et al.* (NA49 Collaboration), *Inclusive production of protons, anti-protons, neutrons, deuterons and tritons in p+C collisions at 158 GeV/c beam momentum*, Eur. Phys. J. C **73**, 2364 (2013).
- [60] H. Adhikary *et al.* (NA61/SHINE Collaboration), *Measurement of hadron production in  $\pi^-$ -C interactions at 158 and 350 GeV/c with NA61/SHINE at the CERN SPS*, Phys. Rev. D **107**, 062004 (2023).
- [61] H. Adhikary *et al.* (NA61/SHINE Collaboration), *Evidence of isospin-symmetry violation in high-energy collisions of atomic nuclei*, Nature Commun. **16**, 2849 (2025).
- [62] S. Ostapchenko and G. Sigl, *On the model uncertainties for the predicted muon content of extensive air showers*, Astropart. Phys. **163**, 103004 (2024).
- [63] A. Aduszkiewicz *et al.* (NA61/SHINE Collaboration), *Measurement of meson resonance production in  $\pi^-$ -C interactions at SPS energies*, Eur. Phys. J. C **77**, 626 (2017).
- [64] J. Whitmore, S. J. Barish, D. C. Colley, and P. F. Schultz, *Invariant cross-section for the inclusive reaction  $p + p \rightarrow p + X$  at 205 GeV/c*, Phys. Rev. D **11**, 3124 (1975).
- [65] I. V. Ajinenko *et al.* (EHS/NA22 Collaboration), *Strange and nonstrange baryon production in  $\pi^+p$  and  $K^+p$  interactions at 250 GeV/c*, Z. Phys. C **44**, 573 (1989).
- [66] F. Oljemark, *Single Diffraction in proton-proton scattering with TOTEM at the Large Hadron Collider*, PhD thesis, University of Helsinki (2020).
- [67] A. Aduszkiewicz *et al.* (NA61/SHINE Collaboration), *Measurements of  $\pi^\pm$ ,  $K^\pm$ ,  $p$  and  $\bar{p}$  spectra in proton-proton interactions at 20, 31, 40, 80 and 158 GeV/c with the NA61/SHINE spectrometer at the CERN SPS*, Eur. Phys. J. C **77**, 671 (2017).
- [68] A. Aduszkiewicz *et al.* (NA61/SHINE Collaboration), *Measurements of hadron production in  $\pi^+ + C$  and  $\pi^+ + Be$  interactions at 60 GeV/c*, Phys. Rev. D **100**, 112004 (2019).
- [69] M. Apollonio *et al.* (HARP Collaboration), *Forward production of charged pions with incident protons on nuclear targets at the CERN PS*, Phys. Rev. C **80**, 035208 (2009).
- [70] M. Apollonio *et al.* (HARP Collaboration), *Forward production of charged pions with incident  $\pi^\pm$  on nuclear targets measured at the CERN PS*, Nucl. Phys. A **821**, 118 (2009).
- [71] G. Aad *et al.* (ATLAS Collaboration), *Charged-particle multiplicities in pp interactions measured with the ATLAS detector at the LHC*, New J. Phys. **13**, 053033 (2011).
- [72] G. Aad *et al.* (ATLAS Collaboration), *Charged-particle distributions in  $\sqrt{s} = 13$  TeV pp interactions measured with the ATLAS detector at the LHC*, Phys. Lett. B **758**, 67 (2016).

- [73] O. Adriani *et al.* (LHCf Collaboration), *Measurements of longitudinal and transverse momentum distributions for neutral pions in the forward-rapidity region with the LHCf detector*, Phys. Rev. D **94**, 032007 (2016).
- [74] O. Adriani *et al.* (LHCf Collaboration), *Measurement of inclusive forward neutron production cross section in proton-proton collisions at  $\sqrt{s} = 13$  TeV with the LHCf Arm2 detector*, J. High Energy Phys. **11**, 073 (2018).
- [75] T. Bergmann, R. Engel, D. Heck, N. N. Kalmykov, S. Ostapchenko, T. Pierog, T. Thouw, and K. Werner, *One-dimensional hybrid approach to extensive air shower simulation*, Astropart. Phys. **26**, 420 (2007).
- [76] T. Pierog and K. Werner, *EPOS LHC-R : a global approach to solve the muon puzzle*, PoS **ICRC2025**, 358 (2025).
- [77] H. Fesefeldt, *The simulation of hadronic showers: physics and applications*, Report PITHA-85/02 (1985), RWTH Aachen.
- [78] T. Pierog and K. Werner, *Muon production in extended air shower simulations*, Phys. Rev. Lett. **101**, 171101 (2008).
- [79] G. Battistoni, F. Cerutti, A. Fassò, A. Ferrari, S. Muraro, J. Ranft, S. Roesler, and P. R. Sala, *The FLUKA code: description and benchmarking*, AIP Conf. Proc. **896**, 31 (2007).
- [80] M. Bleicher *et al.*, *Relativistic hadron hadron collisions in the ultrarelativistic quantum molecular dynamics model*, J. Phys. G **25**, 1859 (1999).
- [81] S. S. Ostapchenko, *Contemporary models of high-energy interactions: Present status and perspectives*, J. Phys. G **29**, 831 (2003).
- [82] R. D. Parsons, C. Bleve, S. S. Ostapchenko, and J. Knapp, *Systematic uncertainties in air shower measurements from high-energy hadronic interaction models*, Astropart. Phys. **34**, 832 (2011).
- [83] S. Ostapchenko, M. Bleicher, T. Pierog, and K. Werner, *Constraining high energy interaction mechanisms by studying forward hadron production at the LHC*, Phys. Rev. D **94**, 114026 (2016).
- [84] S. Ostapchenko, *LHC data on inelastic diffraction and uncertainties in the predictions for longitudinal extensive air shower development*, Phys. Rev. D **89**, 074009 (2014).
- [85] S. Ostapchenko and M. Bleicher, *Constraining pion interactions at very high energies by cosmic ray data*, Phys. Rev. D **93**, 051501(R) (2016).
- [86] H. J. Drescher, A. Dumitru, and M. Strikman, *High-density QCD and cosmic ray air showers*, Phys. Rev. Lett. **94**, 231801 (2005).
- [87] J. Albrecht *et al.*, *Global tuning of hadronic interaction models with accelerator-based and astroparticle data*, Nat. Rev. Phys. (2025), <https://doi.org/10.1038/s42254-025-00897-3>.
- [88] S. R. Kelner, F. A. Aharonian, and V. V. Bugayov, *Energy spectra of gamma-rays, electrons and neutrinos produced at proton-proton interactions in the very high energy regime*, Phys. Rev. D **74**, 034018 (2006).
- [89] T. Kamae, N. Karlsson, T. Mizuno, T. Abe and T. Koi, *Parameterization of  $\gamma$ ,  $e^\pm$  and neutrino spectra produced by  $p - p$  interaction in astronomical environment*, Astrophys. J. **647**, 692 (2006).

- [90] M. Korsmeier, F. Donato, and M. Di Mauro, *Production cross sections of cosmic antiprotons in the light of new data from the NA61 and LHCb experiments*, Phys. Rev. D **97**, 103019 (2018).
- [91] M. Kachelrieß, I. V. Moskalenko, and S. Ostapchenko, *AAfrag: Interpolation routines for Monte Carlo results on secondary production in proton-proton, proton-nucleus and nucleus-nucleus interactions*, Comput. Phys. Commun. **245**, 106846 (2019).
- [92] L. Orusa, M. Di Mauro, F. Donato, and M. Korsmeier, *New determination of the production cross section for secondary positrons and electrons in the Galaxy*, Phys. Rev. D **105**, 123021 (2022).
- [93] L. Orusa, M. Di Mauro, F. Donato, and M. Korsmeier, *New determination of the production cross section for  $\gamma$  rays in the Galaxy*, Phys. Rev. D **107**, 083031 (2023).
- [94] L. Orusa, M. Di Mauro, and F. Donato, *New determination of the neutrino hadronic production cross sections from GeV to beyond PeV energies*, Phys. Rev. D **113**, 2 (2026).